

# A new sample of OH/IR stars in the Galactic center

L.O. Sjouwerman<sup>1,2</sup>, H.J. van Langevelde<sup>3</sup>, A. Winnberg<sup>1</sup>, and H.J. Habing<sup>2</sup>

<sup>1</sup> Onsala Rymdobservatorium, S-439 92 Onsala, Sweden

<sup>2</sup> Sterrewacht Leiden, P.O. Box 9513, 2300 RA Leiden, The Netherlands

<sup>3</sup> Joint Institute for VLBI in Europe, Radiosterrenwacht Dwingeloo, P.O. Box 2, 7990 AA Dwingeloo, The Netherlands

Received April 14, accepted June 4, 1997

**Abstract.** Two independent, largely overlapping 1612 MHz data sets were searched for OH/IR stars in the Galactic center. One set, taken with the Very Large Array in the period 1988 to 1991, consists of 17 epochs monitoring data of Van Langevelde et al. (1993). The other set was observed in 1994, using the Australia Telescope Compact Array. This article describes the data reduction procedures as well as a different way of searching image cubes for narrow line sources, and lists<sup>1</sup> a total of 155 double peak OH maser detections within 18' or 40 projected parsecs of Sagittarius A\*, the compact radio continuum source in the Galactic nucleus. Presented are 65 formerly unseen double peaked 1612 MHz emitters, of which 52 are OH/IR stars. Also given are 3 single peak sources, which we believe to be masers of OH/IR stars. Apart from being less bright in their 1612 MHz OH maser line, the previously unknown OH/IR stars do not seem to be different from the previously known population of OH/IR stars in the Galactic center. We find that the OH/IR star OH maser luminosity distribution peaks at  $L_{\text{OH}} \approx 10^{43.4}$  photons per second. Further physical and kinematical analysis of the new sample will be presented in additional papers.

**Key words:** masers — catalogs — surveys — stars: AGB and post-AGB — Galaxy: center — radio lines: stars

## 1. Introduction

When a star of low to intermediate main sequence mass ( $1-7 M_{\odot}$ ) has reached the stage where its central part is built up of a degenerate nucleus of carbon and oxygen,

---

Send offprint requests to: L.O. Sjouwerman (Onsala); e-mail: sjouwer@oso.chalmers.se

<sup>1</sup> Tables 2 and 3 are also available in electronic form at CDS via anonymous ftp to cdsarc.u-strasbg.fr (130.79.128.5), or via the WWW at <http://cdsweb.u-strasbg.fr/Abstract.html>. Figures 4 and 5 are only published electronically and obtainable from <http://www.edpsciences.com>

it starts ascending the asymptotic giant branch (AGB) of the Hertzsprung-Russell diagram. While burning hydrogen and helium in a shell around the nucleus it will expand its envelope. The star pulsates and starts losing mass at a high rate ( $10^{-7}$  to  $10^{-4} M_{\odot} \text{ yr}^{-1}$ ). The star will be obscured in the visible wavelengths by its dense shell of circumstellar matter. In this slowly expanding and cooling shell molecules form and with regularity conditions are met, such that the molecules in the circumstellar shell support a maser.

Since the discovery of the double peaked profile of the hydroxyl maser satellite line at 1612 MHz in late-type infrared stars, the so-called OH/IR stars have been studied to investigate stellar evolution and Galactic dynamics. The characteristic double spectral feature originates from hydroxyl (OH) masers in the expanding circumstellar shells of oxygen rich AGB stars. It is easy to recognise the object as an OH/IR star; one obtains the position and line-of-sight velocity of the star as well as the shell expansion velocity directly from the double peaked spectrum.

As the variable stellar radiation at visible and near-infrared wavelengths is absorbed, the only means of investigating the properties of the underlying star is by observing radiation that is re-emitted by the shell: infrared and sub-mm emission of the dust and gas, in which the molecules can show maser emission (OH, H<sub>2</sub>O and SiO). Reviews on the star and its envelope can be found in Iben & Renzini (1983) and in Habing (1996).

Apart from studying the underlying star, one can also make use of OH/IR stars to probe the Galaxy for its structure, evolution and dynamics. For example, Whitelock et al. (1991) derived a period-luminosity relationship similar to the Mira variables and Blommaert et al. (1994) compared the OH/IR stars in the center, bulge and outer part of our Galaxy. Good reviews about using OH/IR stars as tools, are from Habing (1993) and Dejonghe (1993).

## *The Galactic center*

Lindqvist et al. (1992a; hereafter LWHM) surveyed the Galactic Center (GC) region for OH/IR stars with the

Very Large Array (VLA) in 1984 and 1985. The OH/IR stars in the GC are one of the few stellar samples in the GC that can be directly observed despite the enormous visual extinction ( $A_V > 25$  mag) in front of the GC. The total of 150 OH/IR stars found (see appendix) are all at about the same distance and thus can be studied as a sample without assumptions on their individual distances (e.g. Baud et al. 1981; Jones et al. 1994; Blum et al. 1996). In Lindqvist et al. (1992b) the stars are investigated for their spatial and kinematic properties and used as tracers of the central potential and mass distribution. It is shown that the distribution of the GC sample generally depends on the shell expansion velocity at 1612 MHz and that the surface density increases strongly towards Sagittarius A\* (Sgr A\*). Sevenster et al. (1995) have shown that the OH/IR stars in the GC consist of a global Galactic component and a separate, strongly rotating disk of “younger” OH/IR stars, possibly formed at a distinct event. Unfortunately the number of OH/IR stars known is too low to do a conclusive dynamical study, especially within about 10–20 pc of Sgr A\*. Lindqvist et al. (1997) show that there should be many more OH/IR stars in the GC with apparent weak OH masers. The reason why they have not been found in the LWHM survey is mainly a matter of sensitivity. Also the OH masers vary in luminosity, as they are indirectly pumped by the variable stellar radiation. To find all stars one should preferably observe and search the same region for more than one epoch.

By monitoring the variability of some of the LWHM OH sources with the VLA, Van Langevelde et al. (1993; hereafter vLJGHW, or the “monitor”) have tried to measure phase-lag distances to these OH/IR stars in order to get a direct estimate of the distance to the GC. However, a highly scattering interstellar medium was discovered in the direction of the GC, making it impossible to achieve their primary goal (Van Langevelde & Diamond 1991). Nevertheless, 20 observations of the GC region had been done, each in sensitivity comparable to the original LWHM survey observations. A “cheap” way of finding faint OH/IR stars is by analysing the concatenated data set. In that way the search can be done in a high-sensitivity data cube, and one is able to detect OH/IR stars which were in a minimum of their OH maser luminosity at the time of the LWHM survey. By averaging many different epochs taken over a time longer than the typical periods of the stars, the detection becomes effectively a function of the time averaged flux density in the spectral peaks. With 20 epochs, the most sensitive way to find stars is by using the concatenated data rather than to search all epochs separately (under the assumption that the OH/IR stars vary typically a factor of two during the monitor).

We intend to use the new, extended sample of OH/IR stars for testing the location of, and probing the potential in the very center of our Galaxy, and, secondly, to study

the sample of OH/IR stars in the GC compared to all other known samples of OH/IR stars. To overcome asymmetry problems, introduced by the particular pointing of the VLA data (optimised for the monitoring program; see below), we used the Australia Telescope Compact Array (ATCA). The bandwidth for the ATCA observations has been chosen to include an equal sensitive search for high-velocity<sup>2</sup> OH/IR stars (velocity up to 600 km s<sup>-1</sup>), which might add important clues for future dynamical modelling.

#### *Outline of this paper*

In this paper we describe the data reduction procedure of the VLA monitor data set and of the ATCA observations in Sect. 2. Section 3 presents a list of both known and suspected OH/IR stars in the GC. Here, when we refer to an OH/IR star, we actually refer to *circumstellar OH maser emission*. The large interstellar visual extinction prevents us to make a clear distinction between optically thick circumstellar shells, as for genuine OH/IR stars, and optically thin circumstellar shells as for the evolutionary closely related Mira variables. We may even have picked up an individual supergiant; however, see Blum et al. (1996) for recent evidence that the number of supergiants in the GC is low. Section 3 also includes an error budget for our measurements. In Sect. 4, we comment on some of the detections. We discuss the survey sensitivity and anomalous features in some OH/IR star spectra. Briefly, we compare the previously unknown OH/IR stars with the known OH/IR stars and derive the OH luminosity distribution. From this we conclude in Sect. 5, that the central stars of the new detections are not different from the AGB stars that constitute the known population in the GC.

We do not attempt to measure the periods of the individual detections as the objects are too faint to be detected in each epoch separately. Also, detailed discussion of the spatial, kinematic and physical properties of the new, extended sample of OH/IR stars in the GC, as well as the issue whether Sgr A\* is the dynamical center of the OH/IR star sample, is deferred to additional papers. A preliminary result on the survey can be found in Sjouwerman & Van Langevelde (1996).

## **2. Data handling and image analysis**

Table 1 summarises the characteristics of the three different image cubes made; Figure 1 depicts an overview of the sky area surveyed, together with the sensitivity contours thereof.

<sup>2</sup> Stellar velocities in this paper refer to line-of-sight velocities as measured with respect to the local standard of rest reference frame (LSR).

**Table 1.** 1612 MHz survey image cubes

Survey	Image cube center	(epoch)	Size	Resolution	Channel width	RMS	Velocity range
			'	"	km s <sup>-1</sup> kHz	mJy	km s <sup>-1</sup>
a VLA	17 <sup>h</sup> 42 <sup>m</sup> 12 <sup>s</sup> .6 –28°56'18".0	(B1950)	37	2.2	1.14 6.1	7.2	–93→ +176
b VLA	17 <sup>h</sup> 42 <sup>m</sup> 29 <sup>s</sup> .3 –28°59'18".0	(B1950)	17	0.5	2.27 12.2	3.7	–92→ +176
c ATCA	17 <sup>h</sup> 45 <sup>m</sup> 40 <sup>s</sup> .0 –29°00'28".0	(J2000)	37	2.2	1.45 7.8	4.5	–600→ +700

### 2.1. The VLA data catena

The monitor data was in 1992 the most extended, uniform 1612 MHz spectral line data set of the GC known by the authors. We did not consider extending the concatenation with observations by others (Habing et al. 1983; LWHM), because those observations were taken in a period when the VLA was limited in its spectral line capabilities. The observations and data reduction of the monitor data used are described in detail in vLJGHW. We chose to start from their calibrated data sets, mainly because bad visibilities and interference from the Russian GLONASS satellite positioning system had already been removed.

In summary, the  $\approx 4$  GByte of calibrated visibility data sets consist of 20 epochs of two-hour VLA observations, taken in different array configurations in the period from January 1988 to January 1991. Unfortunately for the current project, the sky position is not exactly centered on Sgr A\*, and the velocity coverage is limited to only  $-110$  to  $+190$  km s<sup>-1</sup>. The data have been reduced, calibrated and analysed using the NRAO AIPS reduction package (versions from 15JAN88, up to 15JUL94), which we continued to use on the concatenated data set. Being forced to use different AIPS versions over the years introduced some problems with the data tables during the concatenation process. We will comment on that below. We are confident that the final results are not different from what could have been obtained if we had started with the raw visibility data and performed the concatenation in one AIPS version only.

#### 2.1.1. Initial VLA data set selection

The following steps were taken for each individual data set to ensure the homogeneity of the sets, before concatenating them to one visibility file for final processing.

Each of the calibrated monitor data sets was checked for consistency by fully imaging a couple of known strong OH sources. Because of different problems, three epochs had to be regarded lost for our project. We did not process the raw data, as a few missing epochs would not make a significant difference in the noise statistics or detection probabilities. Also, due to inconsistent removal of interference in several epochs, we did not use any of the visibility data which could have been affected. Therefore, all data

for which the baselines were shorter than  $3$  k $\lambda$  was disregarded. If necessary, the  $u, v, w$  vectors were recalculated to have the coordinates (B1950) RA 17<sup>h</sup>42<sup>m</sup>12<sup>s</sup>.600 and DEC  $-28^{\circ}58'18''.00$  as phase center.

The largest effect of using different AIPS versions could be seen in some tables containing additional information to the data. We mainly had to deal with the flagging tables as the table format had changed. It was impossible to restore the original flagging, so for each combination of baseline and time in a flagging table, all visibility information was marked as bad data. Whenever applying the task SPLIT, the sky frequency (different for each epoch) and velocity information in each header and antenna file got reset and had to be repaired by hand. As we will not use frequencies (but velocities instead) and the velocity consistency had already been checked with spectra and maps, we took an arbitrary file header and used it to set all the relevant values to match. The same was done for the frequency information in the antenna file. By doing this, one introduces an error less than 0.05%, in appearance comparable to radial bandwidth smearing, but in net effect negligible. At this time the data sets were also converted from circular polarisations to Stokes “I” to reduce the file sizes with a factor of two immediately.

As the absolute flux calibration of each data set had been done carefully by vLJGHW for the flux monitoring program, we have not performed any further bandpass or amplitude correction, visibility phase recalculation or flagging operation on the individual monitor data sets.

#### 2.1.2. Concatenated VLA data set processing

All data sets were added in a similar manner to create one concatenated visibility data set of about 35 observing hours. Each epoch was put in a different sub-array without rescaling the visibility weights. Due to different calibration paths, the individual weights of the visibility points differed per monitor data set. To get each epoch contribute equally, we treated all visibility weights to be unity. Although formally one has to account for the epochs that are taken in one polarisation only (two data sets before August 1988), we have not looked into this matter after converting each data set to Stokes “I”.

To subtract confusing continuum emission, a baseline was fitted to each visibility spectrum, using three regions

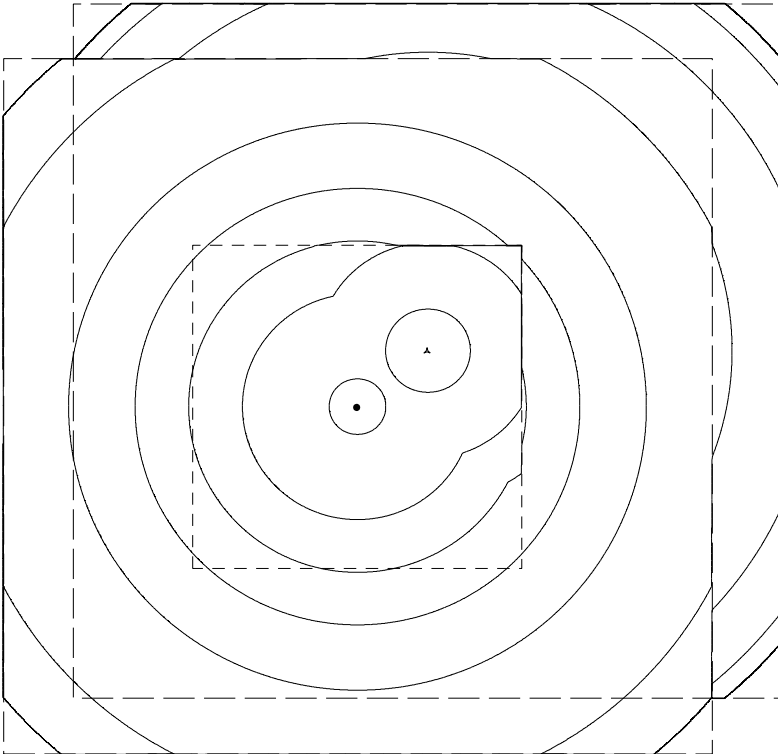


**Fig. 1.** Composite survey area. The filled circle represents the position of Sgr A\*, as well as the center for both the high resolution VLA and the ATCA image cubes. The triangle represents the image cube center for the concatenated VLA monitor data. Long-dashed squares are the 37' VLA and ATCA surveys; we filtered out the corners for which the distance to the field (pointing) center was larger than 24'. The short-dashed square encloses the high resolution, 17' VLA image. Drawn in solid lines are contours of equal detection probability; lines connecting points with equal sensitivity, according to the most sensitive image cube, after correcting for the primary beam attenuation (thus acting as a “primary beam response” for this combined survey). Contours drawn are, from inside out, 1.005, 1.1, 1.25, 1.5, 2, 4, 8 and 16 times 25 mJy. Note that the VLA beam degrades faster because of a larger dish size; the VLA has 25 meter, the ATCA has 22 meter dishes. Approximate J2000 corner coordinates are: upper right  $17^{\text{h}}44^{\text{m}}05^{\text{s}} -28^{\circ}40'31''$  to lower left  $17^{\text{h}}47^{\text{m}}06^{\text{s}} -29^{\circ}19'02''$

in the total spectral band which seemed to be void of line sources (Van Langevelde & Cotton 1990; Cornwell et al. 1992). Several channels of each region were averaged, and interpolated to represent the continuum emission. This visibility model for the continuum emission was subtracted from all channels of the concatenated VLA data set. On the fly, all visibility points exceeding twice the expected flux in the channel with the strongest source, were clipped. For epoch alignment we used a single self-cal iteration on the visibility phases. It corrects for *relative* systematic (atmospheric) effects in the different monitor data sets. We selected the red shifted peak of OH359.938–0.077; a single channel with only one strong, 6 Jy peak, and close to the field center.

From this calibrated visibility data set we made two naturally weighted image cubes and a number of “clean boxes”; strong sources outside the main image cube were mapped in small fields to limit their side-lobe interference. The first image cube is a full primary beam, low spatial, but full frequency resolution image cube (survey “a” in Table 1). The next is a small field, high spatial resolution image cube (“b”) of the same VLA data set, for which we averaged two channels. The latter was centered on Sgr A\* and the – not fully removed – extended continuum emission of the Sgr A complex. The low resolution image was chosen to match the spatial resolution of the ATCA. The large pixel size resulted in having only the shorter baselines (about one half of the 550 000 visibilities) contribute to the image, whereas for the high resolution

image cube, about 90% of the visibilities could be used. Using an even higher resolution, to allow all visibilities to be used, would result in huge maps or alternatively too many “clean boxes” (more than 15). It would thus require an extra pass of subtraction of sources, without a substantial decrease in noise level. The numbers used were a trade-off between resolution, noise level, sky coverage, execution time and disk usage. For reference, to map the entire region at full spatial and spectral resolution would require at least 34 Gb of disk space (with our choices less than 4), and because the execution time is strongly dependent on the disk I/O speed, even with modern workstations it would take months to execute (compared to a handful of days). Effectively, only the baselines between 4 and 32.2 k $\lambda$  and 4 and 143.8 k $\lambda$  were used for the low and high spatial resolution images, respectively. Fitted RMS noise levels per channel were measured to be 7.2 and 3.7 mJy on average, respectively.

## 2.2. ATCA observations and data reduction

The ATCA was used on 8, 10, 11 and 13 July 1994. To reduce broadband interference by GLONASS and to filter out as much as possible of the extended continuum emission in the GC region, the longest baseline configuration was selected for all the observations. The GC was observed at a central frequency of 1612.0 MHz, covering 8 MHz bandwidth over 1024 frequency channels. The integration time was about 12 hours for each of the observing days.

To circumvent GLONASS interference in the bandpass calibration, the primary flux calibrator B1934–638 was observed three times per observing run; typically every 6 hours. The phase calibrator B1748–253 was observed roughly every 40 minutes. Once per observing run we also observed the VLA primary flux calibrator B1328+307 to check the consistency of the flux density measurements between the ATCA and VLA. Actually, for July 10th, we used B1328+307 for bandpass calibration, because interference affected all B1934–638 observations of that day.

After removing bad visibility data points and applying the bandpass calibration, the sky-frequencies were converted to LSR velocities. Following the standard phase calibration, the extended continuum emission from compact HII regions and the Sgr A complex was subtracted with a simple two region baseline interpolation in the visibility domain. Excessive amplitude visibilities were clipped before applying one self-calibration iteration solution of the visibility phases, on the same peak and in a similar manner as to the concatenated VLA data set. Again we used “clean boxes” for removing side-lobes of strong sources outside the main image cube. To avoid remaining effects of interference by GLONASS and the subtracted continuum emission of the Sgr A complex in the image cube, we only used baselines exceeding 4 k $\lambda$ . Because of the large amount of disk space required (5 MB per channel), full resolution images were made by the hundred for channels 69 to 964 (–600 to 700 km s<sup>–1</sup>). The RMS noise level is about 4.5 mJy on average.

Because we used self-cal to align different observing days after we had removed all continuum emission from the data, all positions of the OH/IR stars changed with respect to Sgr A\*. Therefore, the channel with the maser line we used for self-cal, was mapped from the unsubtracted calibrated ATCA data set. In this map, the positions of Sgr A\* and the line were measured, after which the maser positions with respect to Sgr A\* could be determined. The same was done for one of the A-array VLA monitor data sets. The positional offsets with respect to Sgr A\* in Table 2 link both VLA and ATCA observations together.

### 2.3. Image cube analysis

In order to search for discrete line sources, each of the three dimensional image cubes was projected into one two dimensional image in the following way: for each pixel in the sky plane, the maximum intensity over the whole frequency/velocity axis was stored in a new, two dimensional sky image. We shall refer to this image as the “maxmap”. In that way one gets an overall view of the sky location of intensity maxima, although without directly knowing the velocity corresponding to the peaks. The “maxmap” resembles a continuum image (but recall that we already have filtered out the continuum emission), but with a much higher signal to noise ratio than if we would have av-

eraged the pixel intensities over all channels. Alternatively, one can make a total intensity map (or “zeroth order map”); an image for which the flux densities that are higher than the threshold are integrated over the feature. However, as the total intensity map takes into account every pixel above a certain threshold – and thus indeed would be very useful when looking for double peaked features – it is also very sensitive to broad line sources anywhere in the spectrum. Because we have to deal with the remains of the extended continuum emission of the Sgr A complex, we observe a vast amount of broad line sources (see also Fig. 8). These sources cause severe problems in searching the GC area; from non-linear spectral slopes to different noise and detection statistics. With this in mind, we prefer to use the “maxmap” instead of the total intensity map concept. The final results in both methods do not differ much, but the search is much more straightforward in the “maxmap”.

Resulting were three “maxmaps” that all have the same noise level for the detection of sources as the original image cubes, but now consisting of pixels containing sources and the high-end part of the noise distribution of the original map (i.e. only positive values around and above the RMS noise level; comparable to a Rayleigh noise distribution with a constant offset). Now, instead of searching the original image cubes in each channel separately, and finding each source in several channels, one obtains the same detections by searching the (one channel) “maxmap” only. The “maxmaps” were searched for pixels with intensities over 40 mJy ( $5.5\sigma$ ), 25 mJy ( $6.7\sigma$ ) and 25 mJy ( $5.5\sigma$ ) for the VLA 37', VLA 17' and the ATCA 37' image cubes, respectively. Pixels were then grouped in “islands” and for each “island”, the spectrum in the original image cube was taken at the position with the highest pixel value.

The major advantage is that one would only get one spectrum for each “island” (e.g. 7000 pixels make 200 islands, thus only 200 spectra), risking that one could miss a second object that is spatially adjacent to the object whose spectrum is drawn. Chances of missing a star are higher close to stronger sources (having larger “islands”, beam area) and close to the remnants of improperly removed continuum features of the Sgr A complex (non-linear spectral slopes). Therefore we checked individual pixels of the local maxima in the confused area of the central 5' by hand. We think we might have missed only a couple of objects in our total analysis. The expectation value for two sources to be positionally coincident is less than 1% over the data set, but on the other hand we cannot correct for sources submerged in areas of absorption, or the bowl of negative emission caused by the extended background. The spectra were inspected for a second peak, which we required to be at least  $4.5\sigma$  (respectively 32.4, 16.6 and 20.2 mJy observed flux density) and within the interval of 5–80 km s<sup>–1</sup> of the first peak.

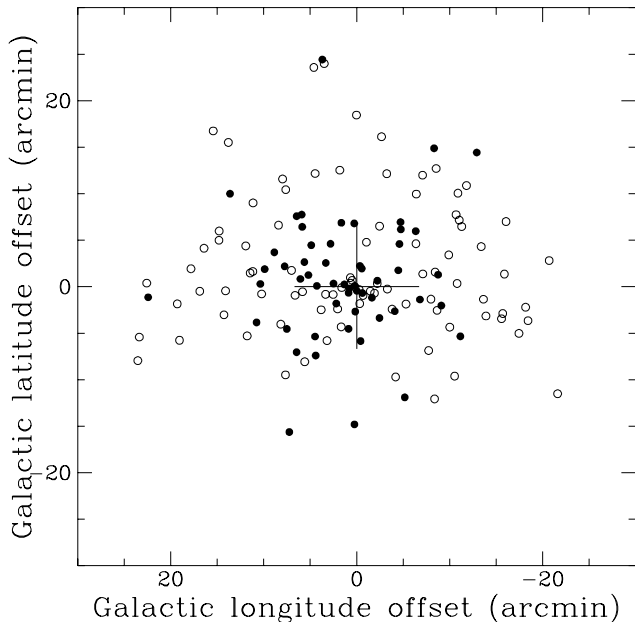


**Fig. 2.** Sky distribution. Closed symbols are new detections, open symbols the previously known OH/IR stars re-detected in this survey. The offsets refer to Sgr A\* ( $\Delta l$ ,  $\Delta b$  in Table 2). Note that the overall concentration of the new detections toward the center is partly due to the “survey beam response” (Fig. 1); the concentration in the very center is however real

### 3. Results

Figures 2 and 3 summarise our results, where it should be noted that the stronger (previously known) sources can be detected further out from the pointing center because of the drop in sensitivity. Tables 2 and 3 (also available electronically through CDS) list all detections within the surveyed area, also when it concerns a previously known source. Figures 4 and 5 (*only* available electronically through CDS) display the 1612 MHz OH maser spectra of all sources. Single peak or suspected double peak detections with a peak flux exceeding  $8\sigma$  (36 mJy before correction in the ATCA data), are also listed. However, we do not list any of the obvious single peaks in the region where confusion with the extended continuum emission occurs. These detections are probably not of stellar origin. This means we have excluded all single peak detections within the box defined by  $l \in [359.92, 359.99]$ ,  $b \in [-0.08, -0.03]$ , even when the peak flux exceeds 36 mJy. Actually, some of the double peak detections in this region might be debatable for being stellar sources. Such cases are indicated in Table 3. In case of a failure detecting the second peak, we usually took the velocity of the second peak from our VLA/ATCA data, or else from LWHM.

For each detection, at the red and blue shifted peaks, fluxes and velocities were determined. The position, together with the formal errors were measured with the

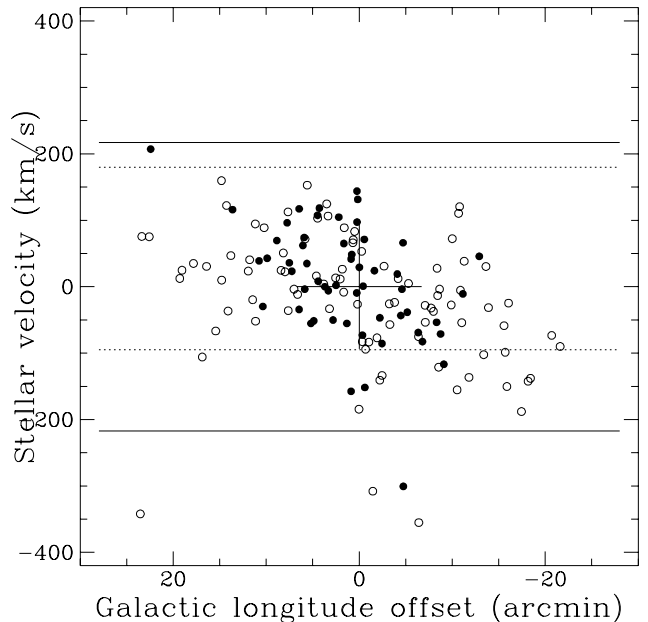


**Fig. 3.** Velocity distribution. Symbols as in Fig. 2. The dotted lines outline the limited coverage of the monitor; the solid lines the velocity interval covered by LWHM

AIPS fitting program IMFIT, in the channel with the highest peak flux. For the VLA data, J2000 positions and Galactic coordinates ( $l$ ,  $b$ ) were calculated from the B1950 positions and then truncated according to the IAU convention. The Galactic coordinates from the ATCA data were calculated after the inverse transformation from J2000 to B1950. All positional and kinematic data of the detections are given in Table 2. Table 3 lists corresponding physical data to each entry in Table 2. Where appropriate, we first list the VLA (“a”, or “b”) and secondly the ATCA (“c”) data. If seen in both the low and high resolution VLA image cubes, we used the high resolution (“b”) result for the position (Table 2) and the low resolution (“a”) result for the velocity and flux information (Tables 2 and 3 and Fig. 4); the other result was used as consistency check in such cases.

As the fluxes measured for the VLA data are averages over 17 observations and depend on the resolution, we show VLA and ATCA spectra separately in Fig. 4 and in Fig. 5. There are considerable difficulties when reaching such low noise levels in the GC area; residuals of the extended OH absorption, continuum subtraction, and very strong maser sources cause poor baselines in both the VLA and ATCA data. Therefore, at the position of the star in the image cube and avoiding the region of the stellar maser emission, a linear baseline was fitted to, and subtracted from the spectrum.

**Table 2.** OH/IR stars in the Galactic center: positional and kinematic data

	OH Name	R. A. and Declination J2000.0			$\delta^{\max}$ "	$V_{\text{blue}}$ $\text{km s}^{-1}$	$V_{\text{red}}$ $\text{km s}^{-1}$	$V_{\text{star}}$ $\text{km s}^{-1}$	$\Delta l$ '	$\Delta b$ '	Ref.
c	359.583−0.239	17 45 33.497	−29 24 57.82	0.096	−103.8	−76.2	−90.0	−21.607	−11.505	1 (13)	
c	359.598−0.000	17 44 39.612	−29 16 46.27	0.167	−92.1	−54.4	−73.3	−20.698	2.814	1 (14)	
c	359.636−0.108	17 45 10.357	−29 18 11.81	0.233	−160.4	−115.4	−137.9	−18.420	−3.650	1 (17)	
c	359.640−0.084	17 45 5.324	−29 17 13.50	0.648	−157.5	−127.0	−142.3	−18.163	−2.206	1 (18)	
c	359.652−0.131	17 45 18.051	−29 18 4.75	0.381	−208.4	−167.7	−188.0	−17.450	−5.021	1 (19)	
a	359.675+0.070	17 44 34.321	−29 10 31.77	0.336	−42.9	−6.5	−24.7	−16.057	7.005	1 (21)	
c	359.676+0.069	17 44 34.492	−29 10 37.34	0.094	−42.8	−6.4	−24.6	−16.040	6.981	1 (21)	
c	359.678−0.025	17 44 56.832	−29 13 25.39	0.141	−172.1	−128.5	−150.3	−15.885	1.359	1 (22)	
a	359.681−0.095	17 45 13.695	−29 15 21.73	0.389	−118.3	−79.2	−98.7	−15.688	−2.844	1 (23)	
c	359.681−0.095	17 45 13.854	−29 15 28.49	0.140	−118.3	−79.1	−98.7	−15.703	−2.881	1 (23)	
c	359.683−0.105	17 45 16.352	−29 15 39.41	0.423	−76.2	−41.3	−58.7	−15.575	−3.441	1 (24)	
a	359.711−0.100	17 45 19.159	−29 13 59.82	0.466	−50.8	−12.2	−31.5	−13.901	−3.148	1 (25)	
c	359.711−0.100	17 45 19.329	−29 14 6.06	0.093	−51.5	−12.2	−31.9	−13.912	−3.184	1 (25)	
a	359.716−0.070	17 45 12.792	−29 12 49.26	0.345	8.2	52.5	30.4	−13.624	−1.351	1 (26)	
c	359.716−0.070	17 45 12.931	−29 12 54.88	0.129	8.1	51.7	29.9	−13.623	−1.373	1 (26)	
c	359.720+0.025	17 44 51.266	−29 9 44.94	0.275	−124.1	−80.5	−102.3	−13.385	4.314	1 (27)	
a	359.728+0.193	17 44 12.900	−29 3 57.50	0.530	30.9	60.4	45.7	−12.907	14.430		
c	359.746+0.134	17 44 29.422	−29 4 58.57	0.216	−144.4	−128.5	−136.5	−11.805	10.879	1 (29)	
a	359.755+0.061	17 44 47.819	−29 6 44.73	0.645	19.6	57.0	38.3	−11.290	6.471	1 (31)	
c	359.755+0.061	17 44 47.953	−29 6 48.03	0.354	19.7	57.5	38.6	−11.249	6.472	1 (31)	
c	359.757−0.136	17 45 34.368	−29 12 52.95	1.015	−31.1	9.5	−10.8	−11.143	−5.343		
a	359.759+0.072	17 44 45.759	−29 6 9.83	0.515	−74.6	−33.8	−54.2	−11.029	7.159	1 (32)	
c	359.760+0.072	17 44 45.967	−29 6 13.32	0.475	−74.7	−34.0	−54.4	−10.982	7.144	1 (32)	
a	359.761+0.120	17 44 34.797	−29 4 31.67	0.138	−20.2	9.4	−5.4	−10.887	10.055	1 (33)	
c	359.762+0.120	17 44 34.949	−29 4 35.39	0.042	−19.5	9.5	−5.0	−10.846	10.051	1 (33)	
a	359.763−0.041	17 45 12.917	−29 9 31.55	0.345	107.0	134.2	120.6	−10.798	0.346	1 (34)	
c	359.763−0.042	17 45 13.032	−29 9 35.95	0.327	106.9	134.5	120.7	−10.782	0.338	1 (34)	
a	359.765+0.082	17 44 44.283	−29 5 33.63	0.738	91.1	129.7	110.4	−10.684	7.748	1 (35)	
c	359.765+0.082	17 44 44.386	−29 5 38.81	0.765	95.3	128.7	112.0	−10.670	7.740	1 (35)	
c	359.767−0.208	17 45 52.594	−29 14 32.55	0.639	−174.9	−135.7	−155.3	−10.530	−9.619	1 (36)	

Table 2. continued

	OH Name	R.A. and Declination J2000.0				$\delta^{\max}$ "	$V_{\text{blue}}$ km s <sup>-1</sup>	$V_{\text{red}}$ km s <sup>-1</sup>	$V_{\text{star}}$ km s <sup>-1</sup>	$\Delta l$ '	$\Delta b$ '	Ref.
a	359.776-0.120	17 45 33.162	-29 11 18.03		0.282	59.3	85.4	72.3	-10.004	-4.349	1 (37)	
c	359.776-0.120	17 45 33.283	-29 11 23.43		0.117	58.9	85.1	72.0	-10.017	-4.371	1 (37)	
b	359.778+0.010	17 45 3.065	-29 7 10.38		0.235	-48.5	-6.5	-27.5	-9.901	3.416	1 (38)	
c	359.779+0.010	17 45 3.214	-29 7 12.63		0.163	-48.6	-6.4	-27.5	-9.860	3.414	1 (38)	
c	359.791-0.081	17 45 26.297	-29 9 24.63		0.487	-116.8	-116.8	-116.8	-9.097	-2.029	6	
b	359.797-0.025	17 45 14.132	-29 7 18.20		0.300	-90.5	-51.9	-71.2	-8.750	1.286	*	
a	359.799-0.090	17 45 29.347	-29 9 11.97		0.157	-22.4	15.0	-3.7	-8.646	-2.543	1 (40)	
c	359.799-0.090	17 45 29.477	-29 9 16.56		0.110	-22.4	13.9	-4.3	-8.643	-2.560	1 (40)	
c	359.801+0.165	17 44 30.082	-29 1 14.09		0.208	-135.7	-106.7	-121.2	-8.541	12.712	1 (41)	
b	359.802-0.021	17 45 13.769	-29 6 52.93		0.178	-36.0	9.4	-13.3	-8.432	1.574	1 (42)	
c	359.803-0.021	17 45 13.911	-29 6 55.80		0.407	-35.5	9.5	-13.0	-8.407	1.566	1 (42)	
c	359.803-0.248	17 46 7.306	-29 13 58.00		0.279	9.5	45.9	27.7	-8.373	-12.064	1 (43)	
a	359.804+0.201	17 44 22.112	-28 59 48.62		0.555	-72.4	-34.9	-53.6	-8.318	14.886	1a (5)	
c	359.805+0.200	17 44 22.320	-28 59 54.71		0.633	-71.8	-34.0	-52.9	-8.300	14.852	1a (5)	
b	359.810-0.069	17 45 26.219	-29 8 1.35		0.069	-58.7	-15.6	-37.2	-7.986	-1.340	1 (44)	
c	359.810-0.070	17 45 26.350	-29 8 4.16		0.147	-58.7	-15.2	-36.9	-7.968	-1.347	1 (44)	
a	359.814-0.162	17 45 48.428	-29 10 40.52		0.651	-51.9	-12.2	-32.1	-7.731	-6.866	1 (45)	
c	359.814-0.162	17 45 48.489	-29 10 45.81		0.168	-51.5	-10.8	-31.1	-7.766	-6.884	1 (45)	
b	359.825-0.024	17 45 17.705	-29 5 51.37		0.082	-74.6	-32.6	-53.6	-7.108	1.376	1 (47)	
c	359.825-0.024	17 45 17.822	-29 5 53.53		0.072	-74.7	-32.6	-53.6	-7.078	1.378	1 (47)	
a	359.825+0.153	17 44 36.341	-29 0 16.41		0.262	-45.1	-11.1	-28.1	-7.084	11.992	1 (46)	
c	359.826+0.153	17 44 36.466	-29 0 19.13		0.178	-44.2	-10.8	-27.5	-7.032	12.001	1 (46)	
b	359.829-0.070	17 45 29.129	-29 7 1.72		0.195	-100.9	-64.4	-82.7	-6.806	-1.365		
c	359.830-0.070	17 45 29.255	-29 7 5.17		0.451	-100.9	-64.5	-82.7	-6.799	-1.377		
c	359.836+0.119	17 44 45.898	-29 0 51.03		0.218	-374.0	-336.2	-355.1	-6.409	9.964	3	
b	359.837+0.030	17 45 6.803	-29 3 31.75		0.117	-82.6	-67.8	-75.2	-6.366	4.621	1 (48)	
c	359.838+0.030	17 45 6.909	-29 3 33.46		0.099	-83.4	-67.4	-75.4	-6.325	4.632	1 (48)	
b	359.837+0.052	17 45 1.580	-29 2 48.21		0.177	-81.4	-56.5	-69.0	-6.344	5.973	1a (6), 6	
c	359.838+0.053	17 45 1.674	-29 2 49.67		0.273	-80.5	-55.8	-68.2	-6.297	5.990	1a (6), 6	
b	359.855-0.078	17 45 34.680	-29 6 0.25		0.067	-16.8	26.4	4.8	-5.299	-1.865	1 (50)	
c	359.855-0.078	17 45 34.784	-29 6 2.88		0.204	-16.6	27.0	5.2	-5.288	-1.868	1 (50)	
c	359.857-0.245	17 46 14.286	-29 11 8.26		0.381	-57.3	-19.5	-38.4	-5.167	-11.896		
c	359.864+0.056	17 45 4.706	-29 1 24.57		0.279	-313.0	-288.3	-300.6	-4.743	6.165	6	



Table 2. continued

	OH Name	R.A. and Declination J2000.0				$\delta^{\max}$ "	$V_{\text{blue}}$ km s <sup>-1</sup>	$V_{\text{red}}$ km s <sup>-1</sup>	$V_{\text{star}}$ km s <sup>-1</sup>	$\Delta l$ '	$\Delta b$ '	Ref.
b	359.864+0.068	17 45	1.705	-29 0	54.29	0.377	46.8	85.4	66.1	-4.710	6.941	6
b	359.867+0.030	17 45	11.149	-29 2	1.98	0.313	-20.2	12.8	-3.7	-4.594	4.592	
c	359.867+0.029	17 45	11.272	-29 2	3.30	0.522	-19.5	13.9	-2.8	-4.547	4.603	
b	359.868-0.018	17 45	22.495	-29 3	24.32	0.207	-62.2	-24.7	-43.4	-4.471	1.761	
c	359.869-0.018	17 45	22.584	-29 3	26.26	0.282	-61.6	-25.3	-43.5	-4.443	1.770	
a	359.873-0.209	17 46	7.999	-29 9	7.92	0.726	-8.8	33.2	12.2	-4.187	-9.709	1 (51)
c	359.872-0.210	17 46	8.083	-29 9	15.21	0.203	-7.9	32.8	12.4	-4.260	-9.758	1 (51)
b	359.875-0.091	17 45	40.589	-29 5	22.66	0.356	5.4	32.6	19.0	-4.091	-2.639	
b	359.880-0.087	17 45	40.379	-29 5	0.95	0.012	-33.8	-13.3	-23.6	-3.806	-2.412	1 (52)
c	359.880-0.087	17 45	40.478	-29 5	3.34	0.047	-34.0	-13.7	-23.9	-3.797	-2.414	1 (52)
b	359.888-0.051	17 45	33.145	-29 3	27.05	0.199	-76.9	-37.2	-57.0	-3.295	-0.248	1 (53)
c	359.888-0.051	17 45	33.212	-29 3	28.85	0.289	-77.6	-36.9	-57.3	-3.274	-0.236	1 (53)
a	359.889+0.155	17 44	44.926	-28 56	54.45	0.227	-40.6	-11.1	-25.8	-3.233	12.151	1 (55)
c	359.890+0.155	17 44	45.032	-28 56	57.95	0.178	-39.8	-12.2	-26.0	-3.196	12.156	1 (55)
a	359.898+0.222	17 44	30.776	-28 54	21.03	0.167	13.9	47.9	30.9	-2.673	16.127	1 (56)
c	359.899+0.222	17 44	30.863	-28 54	24.81	0.079	13.9	48.8	31.3	-2.638	16.134	1 (56)
b	359.902-0.103	17 45	47.321	-29 4	21.50	0.188	-105.2	-65.6	-85.4	-2.453	-3.362	
c	359.902-0.103	17 45	47.408	-29 4	23.43	0.239	-105.2	-66.0	-85.6	-2.448	-3.364	
c	359.902+0.061	17 45	8.830	-28 59	16.62	0.315	-153.2	-113.9	-133.6	-2.455	6.508	1 (57)
c	359.906-0.041	17 45	33.477	-29 2	16.45	0.060	-160.4	-121.2	-140.8	-2.215	0.343	1 (58)
b	359.906-0.036	17 45	32.215	-29 2	3.68	0.137	-67.8	-25.8	-46.8	-2.215	0.650	6, *
c	359.906-0.036	17 45	32.293	-29 2	5.55	0.117	-68.9	-25.3	-47.1	-2.193	0.659	6, *
b	359.911-0.059	17 45	38.199	-29 2	31.71	0.090	-99.4	-55.3	-77.4	-1.932	-0.709	1 (59)
c	359.911-0.059	17 45	38.284	-29 2	33.34	0.423	-99.4	-54.4	-76.9	-1.911	-0.701	1 (59)
c	359.916-0.067	17 45	40.821	-29 2	34.13	1.283	16.8	31.3	24.1	-1.636	-1.183	
c	359.918-0.055	17 45	38.467	-29 2	3.56	0.057	-326.0	-289.7	-307.9	-1.466	-0.477	3
b	359.925+0.032	17 45	18.845	-28 58	56.34	0.201	-95.1	-71.2	-83.2	-1.076	4.771	1 (60)
c	359.926+0.033	17 45	18.925	-28 58	58.03	0.206	-95.1	-71.8	-83.4	-1.045	4.784	1 (60)
c	359.929-0.110	17 45	52.897	-29 3	12.55	0.896	22.6	47.3	35.0	-0.819	-3.776	
c	359.931-0.050	17 45	39.105	-29 1	17.14	1.692	3.7	31.3	17.5	-0.734	-0.193	
b	359.931-0.063	17 45	42.059	-29 1	35.73	0.042	-113.9	-73.5	-93.7	-0.694	-0.943	1 (61)
c	359.932-0.063	17 45	42.135	-29 1	37.56	0.081	-113.9	-74.7	-94.3	-0.683	-0.938	1 (61)

Table 2. continued

	OH Name	R.A. and Declination J2000.0				$\delta^{\max}$ "	$V_{\text{blue}}$ km s <sup>-1</sup>	$V_{\text{red}}$ km s <sup>-1</sup>	$V_{\text{star}}$ km s <sup>-1</sup>	$\Delta l$ '	$\Delta b$ '	Ref.
c	359.932-0.059	17 45 41.324	-29 1 25.61		0.363	-159.0	-144.4	-151.7	-0.605	-0.682	6	
b	359.934-0.059	17 45 41.505	-29 1 23.34		0.672	9.4	30.9	20.1	-0.581	-0.732		
b	359.934-0.015	17 45 31.098	-28 59 57.59		0.398	50.8	91.6	71.2	-0.549	1.953		
a	359.936-0.145	17 46 1.874	-29 3 54.31		0.472	-11.1	12.8	0.8	-0.419	-5.848	1a (7)	
b	359.937-0.010	17 45 30.462	-28 59 37.99		0.246	-95.1	-50.8	-73.0	-0.343	2.242	6	
c	359.938-0.010	17 45 30.544	-28 59 39.26		0.555	-95.1	-51.5	-73.3	-0.311	2.257	6	
b	359.938-0.077	17 45 46.363	-29 1 44.26		0.018	-95.1	-71.2	-83.2	-0.325	-1.819	1 (62)	
c	359.938-0.078	17 45 46.440	-29 1 46.32		0.016	-95.1	-70.4	-82.7	-0.321	-1.819	1 (62)	
b	359.938-0.052	17 45 40.572	-29 0 53.96		0.062	34.3	71.8	53.1	-0.270	-0.303	1 (63)	
c	359.939-0.052	17 45 40.651	-29 0 55.80		0.065	34.2	70.6	52.4	-0.256	-0.297	1 (63)	
c	359.939-0.034	17 45 36.536	-29 0 21.34		0.777	29.9	53.1	41.5	-0.230	0.772	*	
c	359.943-0.055	17 45 41.842	-29 0 48.17		1.939	22.6	35.7	29.2	-0.013	-0.454	*	
c	359.943+0.260	17 44 28.171	-28 50 55.81		0.172	-201.1	-167.7	-184.4	0.024	18.459	1 (64)	
b	359.944-0.068	17 45 45.309	-29 1 10.12		0.998	26.4	42.3	34.3	0.041	-1.326		
c	359.944-0.068	17 45 45.074	-29 1 8.34		1.146	24.1	43.0	33.5	0.065	-1.234		
a	359.946-0.092	17 45 50.856	-29 1 45.48		0.876	114.9	147.8	131.4	0.159	-2.675	6	
c	359.946-0.092	17 45 50.994	-29 1 49.10		0.367	115.6	149.0	132.3	0.154	-2.695	6	
b	359.946-0.075	17 45 46.987	-29 1 12.49		0.412	53.1	87.1	70.1	0.199	-1.660		
b	359.946-0.048	17 45 40.552	-29 0 22.03		0.082	-46.3	-6.5	-26.4	0.182	-0.022	1 (65)	
c	359.946-0.047	17 45 40.628	-29 0 23.47		0.216	-45.7	-6.4	-26.0	0.201	-0.012	1 (65)	
c	359.947-0.294	17 46 38.540	-29 8 1.36		0.431	122.9	165.0	143.9	0.241	-14.807		
b	359.947-0.046	17 45 40.281	-29 0 16.34		0.534	89.4	105.3	97.3	0.232	0.078	*	
b	359.947+0.066	17 45 14.104	-28 56 44.12		0.282	-28.1	9.4	-9.4	0.263	6.805	6	
b	359.951-0.036	17 45 38.535	-28 59 43.88		0.047	69.5	96.8	83.1	0.494	0.685	1 (66)	
c	359.951-0.036	17 45 38.599	-28 59 45.53		0.054	69.1	96.7	82.9	0.512	0.697	1 (66)	
c	359.952-0.058	17 45 43.881	-29 0 26.72		0.579	27.0	45.9	36.4	0.522	-0.649		
b	359.954-0.041	17 45 40.097	-28 59 46.03		0.056	50.2	91.1	70.6	0.642	0.375	1 (67)	
c	359.954-0.041	17 45 40.169	-28 59 47.73		0.023	50.2	90.9	70.6	0.658	0.384	1 (67)	
b	359.954-0.031	17 45 37.873	-28 59 25.16		0.213	46.8	85.4	66.1	0.685	0.971	1 (68)	
c	359.955-0.031	17 45 37.989	-28 59 27.25		1.053	45.9	83.6	64.7	0.704	0.970	1 (68)	

Table 2. continued

	OH Name	R.A. and Declination J2000.0			$\delta^{\max}$ "	$V_{\text{blue}}$ km s <sup>-1</sup>	$V_{\text{red}}$ km s <sup>-1</sup>	$V_{\text{star}}$ km s <sup>-1</sup>	$\Delta l$ '	$\Delta b$ '	Ref.
b	359.956−0.050	17 45 42.654	−28 59 55.65	0.100	35.5	61.6	48.5	0.797	−0.185	4	
c	359.956−0.050	17 45 42.713	−28 59 58.85	0.836	34.2	60.4	47.3	0.787	−0.189	4	
c	359.957−0.123	17 45 59.866	−29 2 12.16	0.695	−157.5	−157.5	−157.5	0.876	−4.535	6	
c	359.957−0.069	17 45 47.276	−29 0 30.18	1.029	51.7	66.2	58.9	0.857	−1.315		
b	359.958−0.058	17 45 44.690	−29 0 6.49	0.519	32.6	50.8	41.7	0.875	−0.659		
b	359.959−0.078	17 45 49.498	−29 0 39.90	0.711	55.9	75.2	65.5	0.949	−1.845		
c	359.959−0.078	17 45 49.601	−29 0 40.79	1.122	51.7	70.6	61.1	0.968	−1.842		
c	359.959−0.067	17 45 47.140	−29 0 20.63	1.222	29.9	56.0	43.0	0.978	−1.206		
b	359.965−0.043	17 45 42.258	−28 59 15.24	0.306	−73.5	−37.2	−55.3	1.327	0.240	*	
b	359.970−0.049	17 45 44.250	−28 59 11.39	0.245	83.1	94.5	88.8	1.609	−0.098	1 (69), *	
b	359.970−0.047	17 45 43.741	−28 59 7.77	0.624	34.9	53.1	44.0	1.603	0.028		
c	359.970−0.047	17 45 43.915	−28 59 8.92	1.370	37.1	57.5	47.3	1.633	0.020		
b	359.971−0.119	17 46 0.869	−29 1 20.58	0.067	−28.1	11.6	−8.2	1.665	−4.319	1 (70)	
c	359.970−0.119	17 46 0.936	−29 1 23.24	0.110	−28.2	11.0	−8.6	1.648	−4.331	1 (70)	
b	359.970+0.067	17 45 17.163	−28 55 30.90	0.214	47.9	82.0	65.0	1.653	6.871	1a (8)	
c	359.971+0.068	17 45 17.208	−28 55 32.04	0.280	47.3	82.2	64.7	1.690	6.896	1a (8)	
a	359.972−0.046	17 45 43.904	−28 59 0.29	1.217	40.0	53.6	46.8	1.716	0.055		
a	359.973+0.162	17 44 55.513	−28 52 24.03	0.306	2.5	50.2	26.4	1.821	12.530	1 (71)	
c	359.974+0.162	17 44 55.600	−28 52 27.98	0.630	2.3	50.2	26.3	1.847	12.534	1 (71)	
a	359.974−0.058	17 45 47.056	−28 59 14.84	1.264	30.9	62.7	46.8	1.869	−0.659		
c	359.974−0.058	17 45 47.012	−28 59 15.80	0.583	24.1	61.8	43.0	1.886	−0.619		
b	359.977−0.087	17 45 54.260	−29 0 0.58	0.030	−5.4	28.6	11.6	2.051	−2.392	1 (72)	
c	359.977−0.087	17 45 54.328	−29 0 2.85	0.066	−5.0	28.4	11.7	2.043	−2.398	1 (72)	
b	359.980−0.077	17 45 52.322	−28 59 34.58	0.118	85.4	124.0	104.7	2.200	−1.805	5	
c	359.980−0.077	17 45 52.395	−28 59 36.47	0.157	85.1	124.3	104.7	2.199	−1.807	5	
b	359.985−0.061	17 45 49.358	−28 58 47.40	0.042	−6.5	33.2	13.3	2.533	−0.843	1 (73)	
c	359.985−0.061	17 45 49.420	−28 58 49.44	0.039	−6.4	32.8	13.2	2.533	−0.842	1 (73)	
b	359.985−0.042	17 45 44.678	−28 58 12.65	0.182	−9.9	13.9	2.0	2.494	0.332	*	
c	359.985−0.041	17 45 44.710	−28 58 13.56	0.374	−13.7	13.9	0.1	2.510	0.351	*	
b	359.990+0.030	17 45 28.729	−28 55 42.18	0.087	−69.0	−31.5	−50.2	2.813	4.614	*	
c	359.990+0.030	17 45 28.801	−28 55 43.81	0.167	−68.9	−32.6	−50.7	2.841	4.628	*	
b	359.996−0.144	17 46 10.260	−29 0 48.33	0.199	−50.8	−15.6	−33.2	3.192	−5.793	1 (74)	
c	359.996−0.144	17 46 10.328	−29 0 51.11	0.248	−50.0	−18.1	−34.0	3.171	−5.808	1 (74)	

Table 2. continued

	OH Name	R.A. and Declination J2000.0			$\delta^{\max}$ "	$V_{\text{blue}}$ km s <sup>-1</sup>	$V_{\text{red}}$ km s <sup>-1</sup>	$V_{\text{star}}$ km s <sup>-1</sup>	$\Delta l$ '	$\Delta b$ '	Ref.
b	359.998-0.005	17 45 37.985	-28 56 20.48	0.081	-25.8	13.9	-6.0	3.325	2.554	6	
c	359.999-0.004	17 45 38.008	-28 56 22.10	0.336	-25.3	13.9	-5.7	3.340	2.574	6	
b	359.999-0.061	17 45 51.216	-28 58 5.03	0.129	88.8	124.0	106.4	3.348	-0.821	1 (75)	
c	359.999-0.061	17 45 51.279	-28 58 7.17	0.293	88.0	124.3	106.2	3.344	-0.823	1 (75)	
a	0.001+0.353	17 44 14.903	-28 44 58.84	0.402	114.9	134.2	124.6	3.493	23.992	1 (76)	
a	0.005+0.360	17 44 13.690	-28 44 34.89	0.791	.0	-71.2	.0	3.694	24.427		
b	0.007-0.089	17 45 58.832	-28 58 32.48	0.131	-19.0	27.5	4.2	3.826	-2.481	1 (77)	
c	0.007-0.089	17 45 58.922	-28 58 34.84	0.174	-19.5	27.0	3.7	3.817	-2.494	1 (77)	
b	0.014-0.046	17 45 49.900	-28 56 48.52	0.219	100.2	136.5	118.3	4.287	0.088	*	
c	0.014-0.046	17 45 49.968	-28 56 49.98	0.458	99.6	135.9	117.8	4.294	0.092	*	
a	0.016-0.171	17 46 19.426	-29 0 35.36	0.597	-11.1	27.5	8.2	4.410	-7.400		
c	0.015-0.171	17 46 19.521	-29 0 41.81	0.340	-12.2	28.4	8.1	4.346	-7.447		
b	0.018-0.137	17 46 11.614	-28 59 28.87	0.188	88.8	126.3	107.5	4.478	-5.357	6	
c	0.017-0.137	17 46 11.679	-28 59 32.15	0.237	89.4	127.2	108.3	4.449	-5.377	6	
a	0.017+0.156	17 45 3.220	-28 50 19.51	0.280	95.6	110.4	103.0	4.474	12.175	1 (78)	
c	0.018+0.156	17 45 3.332	-28 50 23.27	0.354	96.7	109.8	103.2	4.502	12.175	1 (78)	
a	0.020+0.346	17 44 19.169	-28 44 14.53	0.561	-8.8	41.1	16.2	4.612	23.582	1 (79)	
c	0.020+0.346	17 44 19.231	-28 44 21.84	0.801	-7.9	40.1	16.1	4.596	23.565	1 (79)	
b	0.024+0.027	17 45 34.236	-28 54 0.74	0.275	-69.0	-33.8	-51.4	4.886	4.467		
c	0.024+0.027	17 45 34.313	-28 54 1.68	0.830	-68.9	-32.6	-50.7	4.918	4.484		
b	0.029-0.026	17 45 47.528	-28 55 25.84	0.069	-74.6	-36.0	-55.3	5.193	1.248	6?	
c	0.030-0.026	17 45 47.587	-28 55 27.72	0.129	-74.7	-35.5	-55.1	5.196	1.252	6?	
a	0.036-0.182	17 46 24.849	-28 59 55.90	0.688	135.3	170.5	152.9	5.589	-8.071	1 (80)	
c	0.035-0.182	17 46 24.875	-29 0 1.16	0.222	134.5	170.8	152.6	5.532	-8.096	1 (80)	
b	0.037-0.003	17 45 43.104	-28 54 19.81	0.255	29.8	40.0	34.9	5.627	2.647	6	
c	0.037-0.003	17 45 43.162	-28 54 19.94	0.426	29.9	40.1	35.0	5.660	2.669	6	
b	0.040-0.056	17 45 56.036	-28 55 49.46	0.041	50.2	93.3	71.8	5.828	-0.545	1 (81)	
c	0.040-0.056	17 45 56.094	-28 55 51.85	0.067	50.2	92.3	71.3	5.816	-0.551	1 (81)	
b	0.041+0.060	17 45 28.887	-28 52 9.29	0.524	-21.9	14.5	-3.7	5.860	6.434		
a	0.042+0.082	17 45 23.886	-28 51 24.20	0.759	54.8	93.3	74.1	5.917	7.753		
c	0.042+0.082	17 45 23.932	-28 51 26.85	0.721	54.6	93.8	74.2	5.942	7.771		
b	0.044-0.033	17 45 51.196	-28 54 54.50	0.484	41.7	82.6	62.1	6.058	0.835		
a	0.051-0.165	17 46 22.917	-28 58 38.80	0.831	-54.2	-14.5	-34.3	6.467	-7.042	6	
c	0.050-0.165	17 46 22.979	-28 58 44.80	0.144	-54.4	-15.2	-34.8	6.404	-7.080	6	

Table 2. continued

	OH Name	R.A. and Declination J2000.0			$\delta^{\max}$ "	$V_{\text{blue}}$ km s <sup>-1</sup>	$V_{\text{red}}$ km s <sup>-1</sup>	$V_{\text{star}}$ km s <sup>-1</sup>	$\Delta l$ '	$\Delta b$ '	Ref.
a	0.051+0.079	17 45 25.829	-28 51 2.04	0.674	97.9	136.5	117.2	6.455	7.583		
c	0.051+0.079	17 45 25.910	-28 51 5.34	0.299	98.2	135.9	117.0	6.473	7.588		
b	0.053-0.063	17 45 59.430	-28 55 20.66	0.150	-29.2	5.9	-11.6	6.624	-0.929	1 (82)	
c	0.053-0.063	17 45 59.468	-28 55 23.34	0.126	-29.7	6.6	-11.5	6.604	-0.935	1 (82)	
b	0.060-0.018	17 45 49.871	-28 53 37.01	0.047	-23.6	16.2	-3.7	7.009	1.755	1 (83)	
c	0.060-0.018	17 45 49.912	-28 53 39.45	0.084	-23.9	15.4	-4.3	7.000	1.756	1 (83)	
c	0.064-0.308	17 46 58.391	-29 2 27.44	0.566	6.6	40.1	23.3	7.247	-15.628	*	
b	0.068-0.123	17 46 15.651	-28 56 27.83	0.347	19.0	53.1	36.0	7.515	-4.542	6	
c	0.067-0.123	17 46 15.690	-28 56 31.81	0.385	18.3	53.1	35.7	7.470	-4.565	6	
a	0.070+0.127	17 45 17.526	-28 48 32.36	0.212	-54.2	-17.9	-36.0	7.634	10.435	1 (84)	
c	0.070+0.127	17 45 17.565	-28 48 35.93	0.159	-52.9	-18.1	-35.5	7.648	10.447	1 (84)	
a	0.071-0.205	17 46 35.279	-28 58 53.87	0.197	99.0	126.3	112.6	7.657	-9.482	1 (85)	
c	0.070-0.205	17 46 35.321	-28 58 57.14	0.082	99.6	125.8	112.7	7.629	-9.495	1 (85)	
b	0.072-0.011	17 45 49.944	-28 52 45.25	0.324	79.7	112.6	96.2	7.754	2.191		
a	0.076+0.146	17 45 13.848	-28 47 39.09	0.108	1.4	43.4	22.4	7.971	11.585	1 (86)	
c	0.076+0.146	17 45 13.894	-28 47 42.70	0.060	0.8	43.0	21.9	7.988	11.597	1 (86)	
b	0.079-0.114	17 46 15.186	-28 55 38.69	0.156	36.6	65.0	50.8	8.161	-4.030	1 (87)	
c	0.078-0.115	17 46 15.258	-28 55 42.50	0.069	37.1	64.7	50.9	8.124	-4.056	1 (87)	
a	0.083+0.063	17 45 34.222	-28 49 52.45	0.279	4.8	44.5	24.7	8.404	6.619	1 (88)	
c	0.083+0.063	17 45 34.234	-28 49 54.94	0.177	5.2	44.4	24.8	8.420	6.642	1 (88)	
a	0.091+0.014	17 45 46.678	-28 51 0.81	0.569	61.6	77.5	69.5	8.856	3.699		
a	0.108-0.016	17 45 56.219	-28 51 4.16	0.619	21.8	63.8	42.8	9.898	1.888	6	
c	0.107-0.016	17 45 56.267	-28 51 8.42	1.058	21.2	60.4	40.8	9.868	1.875	6	
b	0.113-0.060	17 46 7.405	-28 52 11.75	0.138	71.8	105.8	88.8	10.221	-0.782	1 (90)	
c	0.113-0.061	17 46 7.470	-28 52 15.43	0.163	70.6	105.4	88.0	10.188	-0.804	1 (90)	
a	0.116-0.042	17 46 3.523	-28 51 30.06	0.739	-48.5	-11.1	-29.8	10.363	0.298	6	
c	0.115-0.043	17 46 3.560	-28 51 34.80	0.774	-47.1	-12.2	-29.7	10.321	0.280	6	
a	0.122-0.111	17 46 20.626	-28 53 18.35	0.615	21.8	55.9	38.9	10.769	-3.838		
c	0.121-0.112	17 46 20.736	-28 53 24.98	0.375	21.2	56.0	38.6	10.704	-3.890		
a	0.129-0.020	17 46 0.238	-28 50 6.90	0.340	76.3	112.6	94.5	11.171	1.633	1 (92)	
c	0.128-0.020	17 46 0.305	-28 50 12.00	0.248	76.4	112.7	94.5	11.131	1.608	1 (92)	
a	0.129+0.103	17 45 31.422	-28 46 17.14	0.120	-63.3	-40.6	-51.9	11.146	9.013	1 (91)	
c	0.129+0.103	17 45 31.450	-28 46 21.78	0.082	-63.1	-41.3	-52.2	11.136	9.015	1 (91)	

Table 2. continued

	OH Name	R.A. and Declination J2000.0					$\delta^{\max}$ "	$V_{\text{blue}}$ km s <sup>-1</sup>	$V_{\text{red}}$ km s <sup>-1</sup>	$V_{\text{star}}$ km s <sup>-1</sup>	$\Delta l$ '	$\Delta b$ '	Ref.
a	0.134−0.023	17 46	1.540	−28 49	57.39	0.771	−39.5	0.3	−19.6	11.455	1.472	1 (93)	
c	0.134−0.023	17 46	1.658	−28 49	59.92	0.369	−39.8	−0.6	−20.2	11.456	1.459	1 (93)	
a	0.139−0.135	17 46	28.707	−28 53	11.89	0.847	19.6	61.6	40.6	11.781	−5.293	1 (94)	
c	0.138−0.136	17 46	28.732	−28 53	19.90	0.377	18.3	61.8	40.1	11.684	−5.343	1 (94)	
a	0.142+0.026	17 45	51.293	−28 48	2.09	0.102	0.3	46.8	23.5	11.927	4.388	1 (95)	
c	0.141+0.026	17 45	51.329	−28 48	6.82	0.041	0.8	47.3	24.1	11.893	4.376	1 (95)	
a	0.170+0.119	17 45	33.470	−28 43	39.36	0.789	93.3	138.8	116.0	13.625	10.000		
a	0.173+0.211	17 45	12.423	−28 40	37.70	0.807	29.8	63.8	46.8	13.798	15.516	1 (96)	
a	0.178−0.055	17 46	15.309	−28 48	41.36	0.266	−53.1	−20.2	−36.6	14.107	−0.444	1 (97)	
c	0.177−0.055	17 46	15.347	−28 48	47.86	0.078	−52.9	−19.5	−36.2	14.037	−0.480	1 (97)	
a	0.181−0.098	17 46	25.752	−28 49	53.32	0.546	103.6	141.0	122.3	14.272	−3.021	1 (98)	
c	0.180−0.098	17 46	25.839	−28 49	59.97	0.437	101.1	140.3	120.7	14.202	−3.071	1 (98)	
a	0.189+0.053	17 45	51.857	−28 44	45.50	0.735	−9.9	29.8	9.9	14.789	5.988	1 (99)	
c	0.189+0.052	17 45	51.914	−28 44	51.19	0.079	−9.3	29.9	10.3	14.743	5.964	1 (99)	
a	0.190+0.036	17 45	55.806	−28 45	15.66	0.177	145.6	173.9	159.7	14.814	4.990	1 (100)	
c	0.190+0.036	17 45	55.826	−28 45	18.32	0.066	144.6	173.7	159.2	14.801	4.995	1 (100)	
a	0.200+0.232	17 45	11.488	−28 38	36.27	0.448	−82.6	−50.8	−66.7	15.430	16.753	1 (101)	
c	0.216+0.022	17 46	3.000	−28 44	22.16	0.831	12.4	48.8	30.6	16.416	4.137	1 (103)	
a	0.226−0.055	17 46	22.117	−28 46	15.52	0.475	−122.7	−89.4	−106.0	16.960	−0.455	1 (105)	
c	0.224−0.055	17 46	22.118	−28 46	22.40	0.112	−122.7	−89.2	−105.9	16.878	−0.489	1 (105)	
c	0.240−0.015	17 46	14.952	−28 44	18.67	0.558	16.8	53.1	35.0	17.825	1.927	1 (106)	
c	0.260−0.143	17 46	47.832	−28 47	14.91	0.234	18.3	31.3	24.8	19.053	−5.761	1 (107)	
c	0.264−0.078	17 46	33.125	−28 45	0.79	0.394	−5.0	29.9	12.4	19.292	−1.845	1 (108)	
c	0.317−0.066	17 46	37.780	−28 41	58.06	0.359	194.0	220.2	207.1	22.424	−1.136		
a	0.319−0.041	17 46	32.163	−28 41	1.33	0.117	57.0	93.3	75.2	22.579	0.385	1 (111)	
c	0.321−0.040	17 46	32.132	−28 40	56.17	0.067	57.5	92.3	74.9	22.661	0.457	1 (111)	
c	0.333−0.138	17 46	56.730	−28 43	22.13	1.273	58.9	92.3	75.6	23.380	−5.417	1 (112)	
c	0.335−0.180	17 47	6.964	−28 44	33.03	0.073	−356.5	−327.5	−342.0	23.533	−7.948	2	
1	Lindqvist et al. (1992a) (number) and references therein							4	Levine et al. (1995)				
1a	Lindqvist et al. (1992a), single peak (number)							5	Yusef-Zadeh & Mehringer (1995)				
2	Baud et al. (1975)							6	I.S. Glass, pers. comm. (Glass et al. 1996)				
3	Van Langevelde et al. (1992a)							*	See remarks in main text.				

**Table 3.** OH/IR stars in the Galactic center: physical data

	OH Name	PBF	$S_{\text{blue}}$ mJy	$I_{\text{blue}}$ <sup>a</sup>	$\epsilon$ %	$S_{\text{red}}$ mJy	$I_{\text{red}}$ <sup>a</sup>	$\epsilon$ %	$V_{\text{exp}}$ km s <sup>-1</sup>	$L_{\text{OH}}$ <sup>b</sup>	Deconvolved " "		◦	Note
c	359.583−0.239	8.48	3773.7	19.68	0.2	1460.2	11.22	1.3	13.80	45.1	0.0	0.0	0	
c	359.598−0.000	4.17	383.8	1.31	0.8	517.8	1.31	2.3	18.89	44.0	0.0	0.0	0	
c	359.636−0.108	3.05	541.1	2.36	0.6	229.1	1.70	2.6	22.51	44.2	0.0	0.0	0	
c	359.640−0.084	2.87	35.6	0.10	14.0	175.4	0.33	13.2	15.26	43.2	0.0	0.0	0	LWHM
c	359.652−0.131	2.82	86.1	0.39	3.3	257.5	0.79	4.9	20.33	43.7	0.0	0.0	0	
a	359.675+0.070	2.87	443.0	2.82	0.8	564.3	2.61	2.7	18.16	44.3	4.5	1.8	165	
c	359.676+0.069	2.59	487.8	2.47	0.3	682.0	2.58	0.9	18.16	44.3	0.0	0.0	0	
c	359.678−0.025	2.20	312.0	1.11	0.5	348.0	1.05	1.8	21.79	43.9	0.0	0.0	0	
a	359.681−0.095	3.38	.0	.00	99.0	288.2	0.96	5.8	19.56	43.6	0.0	0.0	0	ATCA
c	359.681−0.095	2.21	255.6	1.67	0.6	595.4	2.17	1.5	19.61	44.2	0.0	0.0	0	
c	359.683−0.105	2.21	120.7	0.41	1.6	43.8	0.14	14.1	17.43	43.3	0.0	0.0	0	
a	359.711−0.100	2.75	200.4	1.00	1.7	288.1	0.95	5.6	19.29	43.9	0.0	0.0	0	
c	359.711−0.100	1.89	402.6	1.46	0.4	576.5	1.89	1.0	19.61	44.1	0.0	0.0	0	
a	359.716−0.070	2.42	229.8	1.55	0.9	318.3	1.74	2.5	22.13	44.1	3.3	2.4	9	
c	359.716−0.070	1.79	390.2	1.71	0.5	525.1	1.99	1.3	21.79	44.2	0.0	0.0	0	
c	359.720+0.025	1.85	164.1	0.55	1.0	12.3	.00	99.0	21.79	43.3	0.0	0.0	0	LWHM
a	359.728+0.193	2.79	118.9	0.06	19.3	54.1	0.05	66.5	14.76	42.6	0.0	0.0	0	
c	359.746+0.134	2.21	168.1	0.37	2.1	287.1	0.62	3.9	7.99	43.6	0.0	0.0	0	
a	359.755+0.061	1.71	130.8	0.66	1.4	78.6	0.61	4.9	18.73	43.7	8.5	1.1	179	
c	359.755+0.061	1.68	123.1	0.33	1.6	86.0	0.38	4.2	18.89	43.4	0.0	0.0	0	
c	359.757−0.136	1.61	39.1	0.10	8.0	52.4	0.11	22.0	20.34	42.9	0.0	0.0	0	
a	359.759+0.072	1.69	96.9	0.92	0.9	123.1	0.76	3.2	20.43	43.8	3.4	2.0	12	
c	359.760+0.072	1.70	149.2	0.67	1.3	137.2	0.59	4.6	20.34	43.7	0.0	0.0	0	
a	359.761+0.120	1.82	1372.4	3.66	1.9	3250.3	9.58	2.3	14.76	44.7	0.0	0.0	0	
c	359.762+0.120	1.96	2305.5	7.50	0.5	7013.8	20.98	0.6	14.53	45.0	0.0	0.0	0	
a	359.763−0.041	1.74	117.5	0.26	3.0	170.1	0.40	5.8	13.62	43.4	0.0	0.0	0	
c	359.763−0.042	1.43	125.6	0.45	1.3	150.5	0.49	3.7	13.80	43.6	0.0	0.0	0	
a	359.765+0.082	1.66	71.8	0.46	1.6	100.0	0.93	2.6	19.30	43.7	0.0	0.0	0	
c	359.765+0.082	1.71	28.1	0.21	3.8	92.6	0.58	4.1	16.71	43.5	0.0	0.0	0	
c	359.767−0.208	1.88	74.0	0.33	2.5	104.4	0.27	9.2	19.61	43.4	0.0	0.0	0	

**Table 3.** continued

	OH Name	PBF	$S_{\text{blue}}$ mJy	$I_{\text{blue}}$ <sup>a</sup>	$\epsilon$ %	$S_{\text{red}}$ mJy	$I_{\text{red}}$ <sup>a</sup>	$\epsilon$ %	$V_{\text{exp}}$ km s <sup>-1</sup>	$L_{\text{OH}}$ <sup>b</sup>	Deconvolved " "		Note <sup>c</sup>
a	359.776−0.120	2.06	453.2	1.07	1.6	193.3	0.51	10.1	13.05	43.8	1.9	1.2	67
c	359.776−0.120	1.44	615.3	1.19	0.7	231.1	0.48	5.7	13.07	43.8	0.0	0.0	0
a	359.778+0.010	1.51	116.0	0.44	1.4	128.4	0.59	3.0	21.00	43.6	0.0	0.0	0
c	359.779+0.010	1.39	195.1	0.46	0.9	181.2	0.61	1.9	21.06	43.6	0.0	0.0	0
c	359.791−0.081	1.30	84.5	0.23	2.0	84.5	0.23	2.0	.00	43.0	0.0	0.0	0
a	359.797−0.025	1.44	55.1	0.16	5.5	70.0	0.24	12.1	19.30	43.2	0.0	0.0	0
a	359.799−0.090	1.67	302.6	1.81	1.2	1013.0	2.71	2.5	18.73	44.2	0.0	0.0	0
c	359.799−0.090	1.27	416.2	2.65	0.5	1041.7	3.87	1.1	18.16	44.4	0.0	0.0	0
c	359.801+0.165	2.06	169.4	0.33	1.6	223.8	0.70	2.4	14.53	43.6	0.0	0.0	0
a	359.802−0.021	1.39	109.5	0.51	1.0	61.5	0.22	6.8	22.70	43.5	0.0	0.0	0
c	359.803−0.021	1.24	76.3	0.38	1.1	47.4	0.08	15.0	22.52	43.3	0.0	0.0	0
c	359.803−0.248	1.95	132.2	2.59	0.8	9.2	.00	99.0	18.16	44.0	0.0	0.0	0 LWHM
a	359.804+0.201	1.97	119.1	0.60	1.2	97.6	0.63	3.4	18.73	43.7	10.8	3.2	2
c	359.805+0.200	2.44	77.3	0.12	7.2	108.4	0.28	9.3	18.89	43.2	0.0	0.0	0
a	359.810−0.069	1.50	250.2	0.98	0.8	134.1	0.70	3.6	21.56	43.8	0.0	0.0	0
c	359.810−0.070	1.21	394.2	1.09	0.7	243.1	0.78	2.9	21.79	43.9	0.0	0.0	0
a	359.814−0.162	2.12	151.8	0.82	1.1	69.3	0.84	3.3	19.86	43.8	9.0	3.9	1
c	359.814−0.162	1.39	181.9	0.64	0.6	82.2	0.39	2.8	20.34	43.6	0.0	0.0	0
a	359.825−0.024	1.28	536.2	2.07	0.6	525.6	2.42	1.6	21.00	44.2	0.0	0.0	0
c	359.825−0.024	1.16	349.6	1.58	0.2	442.2	2.00	0.6	21.06	44.1	0.0	0.0	0
a	359.825+0.153	1.51	220.9	1.07	0.6	136.8	0.70	2.8	17.02	43.8	5.7	2.1	0
c	359.826+0.153	1.81	264.2	0.96	0.6	120.6	0.49	3.4	16.71	43.7	1.7	1.2	35
a	359.829−0.070	1.39	.0	.00	99.0	80.4	0.47	4.5	18.24	43.3	4.0	2.9	45
c	359.830−0.070	1.15	57.2	0.30	1.1	42.9	0.17	5.9	18.16	43.3	0.0	0.0	0 ATCA
c	359.836+0.119	1.53	153.2	0.46	1.0	166.4	0.37	4.0	18.89	43.5	0.0	0.0	0
a	359.837+0.030	1.17	503.8	1.49	0.6	234.2	0.73	3.4	7.38	43.9	0.0	0.0	0
c	359.838+0.030	1.19	520.2	1.80	0.3	228.4	0.70	2.8	7.99	44.0	0.0	0.0	0
a	359.837+0.052	1.18	68.6	0.17	6.7	276.1	0.51	6.8	12.49	43.4	0.0	0.0	0
c	359.838+0.053	1.25	24.9	0.09	4.6	130.8	0.38	3.3	12.35	43.3	0.0	0.0	0
a	359.855−0.078	1.32	119.0	0.57	1.3	198.0	1.21	2.0	21.57	43.8	3.9	0.2	143
c	359.855−0.078	1.09	84.1	0.43	1.1	196.9	0.90	1.5	21.79	43.7	0.0	0.0	0
c	359.857−0.245	1.68	99.8	0.54	1.1	136.0	0.64	2.8	18.89	43.7	0.0	0.0	0
c	359.864+0.056	1.19	89.4	0.26	1.2	25.8	0.15	6.7	12.35	43.2	0.0	0.0	0



Table 3. continued

	OH Name	PBF	$S_{\text{blue}}$ mJy	$I_{\text{blue}}$ <sup>a</sup>	$\epsilon$ %	$S_{\text{red}}$ mJy	$I_{\text{red}}$ <sup>a</sup>	$\epsilon$ %	$V_{\text{exp}}$ km s <sup>-1</sup>	$L_{\text{OH}}$ <sup>b</sup>	Deconvolved " "		◦	Note
a	359.864+0.068	1.11	37.5	0.17	3.5	48.6	0.19	11.0	19.30	43.1	0.0	0.0	0	
a	359.867+0.030	1.08	74.0	0.25	2.8	45.0	0.27	7.9	16.46	43.3	4.8	0.5	5	
c	359.867+0.029	1.12	75.7	0.22	2.2	24.2	0.13	11.4	16.71	43.1	0.0	0.0	0	
a	359.868-0.018	1.11	57.8	0.24	2.4	107.4	0.44	3.8	18.73	43.4	0.0	0.0	0	
c	359.869-0.018	1.06	85.8	0.29	1.3	109.9	0.47	2.4	18.16	43.5	0.0	0.0	0	
a	359.873-0.209	2.34	59.7	0.13	6.8	119.6	0.27	9.6	21.00	43.2	6.5	3.8	38	
c	359.872-0.210	1.41	17.6	0.10	4.0	165.0	0.38	3.3	20.34	43.3	0.0	0.0	0	
b	359.875-0.091	1.31	47.5	0.11	3.6	21.3	0.08	15.5	13.62	42.9	0.0	0.0	0	
a	359.880-0.087	1.28	7608.0	20.20	0.2	2379.7	7.11	1.4	10.22	45.0	0.0	0.0	0	
c	359.880-0.087	1.06	6140.3	20.20	0.2	2161.7	6.41	1.7	10.17	45.0	0.0	0.0	0	
a	359.888-0.051	1.13	100.7	0.66	0.8	111.6	0.59	2.6	19.86	43.7	0.0	0.0	0	
c	359.888-0.051	1.03	55.7	0.48	0.8	104.1	0.50	2.3	20.34	43.6	0.0	0.0	0	
a	359.889+0.155	1.27	109.5	0.60	0.8	169.8	0.61	2.4	14.75	43.7	4.8	2.7	179	
c	359.890+0.155	1.62	185.2	0.76	0.8	295.4	0.93	2.0	13.80	43.8	0.0	0.0	0	
a	359.898+0.222	1.68	326.1	1.73	0.6	446.9	1.94	1.6	17.02	44.2	4.7	1.9	180	
c	359.899+0.222	2.26	495.2	2.31	0.3	806.0	2.62	0.9	17.43	44.3	0.0	0.0	0	
a	359.902-0.103	1.30	.0	.00	99.0	81.3	0.48	4.4	19.82	43.3	0.0	0.0	0	ATCA
c	359.902-0.103	1.05	127.1	0.37	0.9	76.0	0.26	3.9	19.61	43.4	0.0	0.0	0	
c	359.902+0.061	1.14	118.7	0.27	1.5	16.9	0.12	10.5	19.61	43.2	0.0	0.0	0	
c	359.906-0.041	1.01	736.0	2.77	0.3	1200.7	3.52	0.8	19.61	44.4	0.0	0.0	0	
a	359.906-0.036	1.07	52.8	0.10	3.4	210.9	0.64	1.6	21.00	43.5	0.0	0.0	0	
c	359.906-0.036	1.01	77.0	0.20	2.0	287.5	0.70	1.8	21.79	43.5	0.0	0.0	0	
a	359.911-0.059	1.12	.0	.00	99.0	111.4	0.51	3.8	22.03	43.3	0.0	0.0	0	ATCA
c	359.911-0.059	1.01	87.8	0.38	1.2	73.5	0.48	2.8	22.52	43.5	0.0	0.0	0	
c	359.916-0.067	1.01	18.8	0.11	4.8	36.7	0.10	15.0	7.26	42.9	0.0	0.0	0	
c	359.918-0.055	1.01	45.0	0.24	1.4	531.5	2.38	0.4	18.16	44.0	0.0	0.0	0	
a	359.925+0.032	1.00	.0	.00	99.0	162.8	0.56	3.9	11.93	43.3	0.0	0.0	0	ATCA
c	359.926+0.033	1.06	163.8	0.52	1.0	197.5	0.60	2.6	11.62	43.6	0.0	0.0	0	
c	359.929-0.110	1.04	17.9	0.22	1.6	41.6	0.51	2.0	12.35	43.4	7.5	1.6	42	MC?
c	359.931-0.050	1.00	23.0	0.69	0.6	46.4	0.61	2.7	13.80	43.7	15.5	10.6	9	MC
a	359.931-0.063	1.11	.0	.00	99.0	751.9	3.30	0.8	20.20	44.1	2.0	0.5	154	ATCA
c	359.932-0.063	1.00	545.4	2.41	0.3	748.1	3.18	0.7	19.61	44.3	0.0	0.0	0	

Table 3. continued

	OH Name	PBF	$S_{\text{blue}}$ mJy	$I_{\text{blue}}$ <sup>a</sup>	$\epsilon$ %	$S_{\text{red}}$ mJy	$I_{\text{red}}$ <sup>a</sup>	$\epsilon$ %	$V_{\text{exp}}$ km s <sup>-1</sup>	$L_{\text{OH}}$ <sup>b</sup>	Deconvolved " "		◦	Note
c	359.932−0.059	1.00	50.9	0.24	0.9	21.3	0.11	6.3	7.26	43.1	0.0	0.0	0	
a	359.934−0.059	1.10	37.2	1.48	0.3	66.3	1.93	1.2	10.78	44.1	18.4	11.2	26	MC
b	359.934−0.015	1.02	26.0	0.07	5.3	15.6	0.09	14.1	20.43	42.8	0.0	0.0	0	
a	359.936−0.145	1.51	76.2	0.13	4.5	20.4	0.07	25.3	11.92	42.9	0.0	0.0	0	
a	359.937−0.010	1.01	23.1	0.10	99.0	60.4	0.13	13.1	18.73	44.0	0.0	0.0	0	ATCA
c	359.938−0.010	1.01	59.4	0.19	2.1	57.2	0.19	6.5	21.79	43.2	0.0	0.0	0	
a	359.938−0.077	1.15	.0	.00	99.0	6683.5	38.27	0.2	11.93	45.2	0.0	0.0	0	ATCA
c	359.938−0.078	1.01	5783.3	27.93	0.1	6784.0	35.20	0.1	12.35	45.4	0.0	0.0	0	
a	359.938−0.052	1.08	592.5	1.82	0.7	1030.3	2.88	1.3	18.73	44.3	0.0	0.0	0	
c	359.939−0.052	1.00	466.8	1.52	0.5	896.8	2.76	0.8	18.16	44.2	0.0	0.0	0	
c	359.939−0.034	1.00	41.9	0.99	0.3	17.3	0.32	2.7	11.62	43.7	13.5	6.4	174	MC?
c	359.943−0.055	1.00	36.2	0.84	0.7	63.1	0.80	2.9	6.54	43.8	34.6	3.1	157	MC?
c	359.943+0.260	2.87	542.7	1.47	0.8	228.1	0.82	4.0	16.71	43.9	0.0	0.0	0	
a	359.944−0.068	1.11	46.0	4.13	0.1	87.6	4.00	0.3	7.95	44.5	17.1	11.7	12	MC
c	359.944−0.068	1.00	25.9	0.58	1.6	133.6	3.06	1.0	9.44	44.1	17.1	8.9	170	MC
a	359.946−0.092	1.20	31.2	0.19	3.5	46.7	0.20	9.8	16.46	43.2	0.0	0.0	0	
c	359.946−0.092	1.02	21.8	0.06	4.4	52.3	0.14	5.6	16.71	42.9	0.0	0.0	0	
b	359.946−0.075	1.13	37.6	2.06	0.1	15.7	0.92	1.2	17.02	44.1	10.5	3.3	164	MC
a	359.946−0.048	1.06	289.5	2.16	0.6	359.8	1.65	2.6	19.86	44.2	0.0	0.0	0	
c	359.946−0.047	1.00	381.6	3.13	0.4	503.8	2.52	1.7	19.61	44.3	0.0	0.0	0	
c	359.947−0.294	1.97	88.8	0.20	3.2	95.6	0.19	10.0	21.07	43.2	0.0	0.0	0	
b	359.947−0.046	1.06	34.8	0.17	3.3	24.5	0.10	18.0	7.94	43.0	0.0	0.0	0	
a	359.947+0.066	1.00	41.9	0.31	1.9	19.5	0.16	10.7	18.73	43.3	7.0	2.4	36	
a	359.951−0.036	1.04	133.7	0.53	2.9	1012.2	3.67	1.3	13.62	44.2	0.0	0.0	0	
c	359.951−0.036	1.00	102.1	0.48	1.5	1059.3	4.41	0.5	13.80	44.3	0.0	0.0	0	
c	359.952−0.058	1.00	79.3	0.82	0.5	28.0	0.20	6.9	9.44	43.6	9.0	3.1	156	MC?
a	359.954−0.041	1.05	2138.1	9.12	0.2	2641.7	12.04	0.5	20.43	44.9	0.0	0.0	0	
c	359.954−0.041	1.00	2227.4	9.54	0.1	3051.3	13.59	0.2	20.34	45.0	0.0	0.0	0	
a	359.954−0.031	1.03	79.0	0.61	1.0	61.4	0.47	4.0	19.30	43.6	7.2	2.9	5	
c	359.955−0.031	1.00	51.6	0.15	4.4	28.0	0.15	13.0	18.89	43.1	0.0	0.0	0	

Table 3. continued

	OH Name	PBF	$S_{\text{blue}}$ mJy	$I_{\text{blue}}$ <sup>a</sup>	$\epsilon$ %	$S_{\text{red}}$ mJy	$I_{\text{red}}$ <sup>a</sup>	$\epsilon$ %	$V_{\text{exp}}$ km s <sup>-1</sup>	$L_{\text{OH}}$ <sup>b</sup>	Deconvolved " "		◦	Note
a	359.956−0.050	1.07	84.6	0.17	4.3	45.2	0.20	10.9	13.05	43.2	0.0	0.0	0	
c	359.956−0.050	1.00	55.8	0.17	3.4	20.9	0.05	37.7	13.07	42.9	0.0	0.0	0	
c	359.957−0.123	1.06	46.2	0.13	9.7	46.2	0.13	9.7	.00	43.0	0.0	0.0	0	
c	359.957−0.069	1.01	97.1	2.17	0.3	26.8	1.20	1.9	7.26	44.1	20.9	5.3	24	MC
b	359.958−0.058	1.09	27.1	0.23	1.5	31.3	0.25	9.0	9.08	43.3	0.0	0.0	0	
a	359.959−0.078	1.15	54.5	3.33	0.1	47.6	3.23	0.4	9.65	44.4	21.0	12.4	177	MC
c	359.959−0.078	1.01	55.3	0.57	0.9	19.5	0.24	7.0	9.44	43.5	10.9	0.8	154	MC
c	359.959−0.067	1.01	19.3	0.36	1.2	47.7	0.91	1.6	13.08	43.7	23.1	7.2	170	MC
a	359.965−0.043	1.06	57.5	0.18	3.8	42.0	0.20	11.0	18.16	43.2	0.0	0.0	0	
a	359.970−0.049	1.07	36.6	0.65	0.9	51.5	0.62	2.7	5.68	43.7	10.5	4.4	36	
b	359.970−0.047	1.06	30.0	0.74	0.3	16.7	0.41	3.8	9.08	43.6	10.4	1.5	28	MC
c	359.970−0.047	1.01	61.0	0.62	1.3	27.4	0.32	7.4	10.17	43.6	10.1	4.5	176	MC
a	359.971−0.119	1.34	500.1	2.49	0.3	242.8	1.78	1.3	19.86	44.2	0.0	0.0	0	
c	359.970−0.119	1.06	684.1	3.74	0.2	359.6	2.48	1.1	19.61	44.4	0.0	0.0	0	
a	359.970+0.067	1.01	103.5	0.31	2.1	36.2	0.11	18.2	17.03	43.2	0.0	0.0	0	
c	359.971+0.068	1.15	153.0	0.42	1.3	52.0	0.21	8.1	17.43	43.4	0.0	0.0	0	
a	359.972−0.046	1.06	40.9	0.32	2.0	26.5	0.23	8.3	6.81	43.3	9.4	3.6	148	MC
a	359.973+0.162	1.23	79.1	0.32	1.8	142.0	0.41	4.1	23.84	43.4	2.4	2.2	42	
c	359.974+0.162	1.62	65.4	0.25	2.8	107.6	0.28	7.8	23.97	43.3	0.0	0.0	0	
a	359.974−0.058	1.09	24.9	0.77	0.5	46.8	1.19	1.3	15.89	43.9	13.4	7.6	14	MC
c	359.974−0.058	1.01	23.6	0.27	1.1	75.6	1.76	0.6	18.88	43.9	14.5	7.6	167	MC
a	359.977−0.087	1.19	690.8	2.88	0.3	399.5	1.95	1.5	17.03	44.3	0.0	0.0	0	
c	359.977−0.087	1.02	845.3	4.11	0.2	583.8	2.60	0.8	16.71	44.4	0.0	0.0	0	
a	359.980−0.077	1.15	98.8	0.53	1.0	66.3	0.25	6.5	19.29	43.5	3.4	2.2	30	
c	359.980−0.077	1.02	148.9	0.39	0.7	89.7	0.24	3.5	19.61	43.4	0.0	0.0	0	
a	359.985−0.061	1.11	1133.6	5.21	0.4	817.2	3.55	1.8	19.86	44.5	0.0	0.0	0	
c	359.985−0.061	1.02	980.5	5.26	0.1	976.3	4.93	0.3	19.61	44.6	0.0	0.0	0	
a	359.985−0.042	1.06	51.3	0.41	1.0	52.5	0.43	2.8	11.92	43.5	0.0	0.0	0	
c	359.985−0.041	1.01	62.9	0.51	0.7	78.0	0.53	2.0	13.80	43.6	0.0	0.0	0	
a	359.990+0.030	1.00	190.7	0.72	1.4	82.1	0.33	9.1	18.73	43.6	0.0	0.0	0	
c	359.990+0.030	1.08	157.5	0.83	0.4	60.0	0.27	3.5	18.16	43.6	0.0	0.0	0	
a	359.996−0.144	1.53	272.3	0.80	0.9	63.4	0.36	5.9	17.59	43.7	3.4	0.9	149	
c	359.996−0.144	1.13	175.4	0.59	0.8	44.5	0.27	5.4	15.98	43.5	0.0	0.0	0	

Table 3. continued

	OH Name	PBF	$S_{\text{blue}}$ mJy	$I_{\text{blue}}$ <sup>a</sup>	$\epsilon$ %	$S_{\text{red}}$ mJy	$I_{\text{red}}$ <sup>a</sup>	$\epsilon$ %	$V_{\text{exp}}$ km s <sup>-1</sup>	$L_{\text{OH}}$ <sup>b</sup>	Deconvolved " "		Note <sup>c</sup>
a	359.998–0.005	1.03	18.1	0.02	19.0	97.5	0.63	1.9	19.86	43.4	0.0	0.0	0
c	359.999–0.004	1.04	21.8	0.17	1.8	70.7	0.31	3.2	19.61	43.3	0.0	0.0	0
a	359.999–0.061	1.12	102.6	0.87	0.8	90.9	0.47	4.2	17.59	43.7	0.0	0.0	0
c	359.999–0.061	1.03	81.3	0.30	1.1	71.3	0.26	3.9	18.16	43.3	0.0	0.0	0
a	0.001+0.353	4.36	244.6	0.80	2.8	483.4	1.20	5.9	9.65	43.9	5.8	2.6	169
a	0.005+0.360	4.77	.0	.00	99.0	367.3	1.65	6.5	.00	43.8	0.0	0.0	0
a	0.007–0.089	1.23	60.5	0.73	0.8	130.3	0.65	2.7	23.27	43.7	0.0	0.0	0
c	0.007–0.089	1.05	87.6	0.62	0.7	189.6	0.74	1.7	23.24	43.7	0.0	0.0	0
a	0.014–0.046	1.11	23.3	0.16	3.8	103.5	0.49	3.8	18.16	43.4	0.0	0.0	0
c	0.014–0.046	1.05	9.4	.00	99.0	60.9	0.31	5.0	18.16	44.0	0.0	0.0	0 VLA
a	0.016–0.171	1.81	163.2	0.61	2.2	87.3	0.57	7.0	19.30	43.7	0.0	0.0	0
c	0.015–0.171	1.24	112.7	0.64	0.7	58.4	0.46	3.1	20.34	43.6	6.7	0.4	174
a	0.018–0.136	1.53	107.5	0.40	2.5	39.3	0.17	18.7	18.73	43.3	0.0	0.0	0
c	0.017–0.137	1.14	145.2	0.47	0.9	60.5	0.20	6.2	18.89	43.4	0.0	0.0	0
a	0.017+0.156	1.27	127.0	0.40	1.2	140.7	0.33	4.5	7.38	43.5	5.4	3.1	167
c	0.018+0.156	1.66	136.2	0.32	1.9	130.7	0.23	8.3	6.54	43.3	0.0	0.0	0
a	0.020+0.346	4.19	270.5	2.27	0.8	123.4	0.66	8.7	24.97	44.1	0.0	0.0	0
c	0.020+0.346	7.38	481.2	1.30	4.0	262.4	1.31	11.5	23.97	44.0	0.0	0.0	0
a	0.024+0.027	1.05	67.4	0.20	2.4	21.6	0.10	99.0	17.59	42.9	0.0	0.0	0 ATCA
c	0.024+0.027	1.12	45.8	0.13	3.5	9.6	0.07	20.1	18.16	42.9	0.0	0.0	0 VLA
a	0.030–0.026	1.10	110.3	0.57	1.3	169.8	0.65	3.6	19.30	43.7	3.7	0.7	161
c	0.030–0.026	1.08	160.3	0.62	0.5	188.3	0.77	1.1	19.61	43.7	0.0	0.0	0
a	0.036–0.182	1.99	144.0	0.60	1.8	73.4	0.41	8.0	17.60	43.6	0.0	0.0	0
c	0.035–0.182	1.33	164.2	0.62	0.7	56.8	0.28	4.6	18.16	43.5	3.7	1.4	170
a	0.037–0.003	1.09	49.9	0.11	4.7	81.8	0.19	8.6	5.11	43.1	0.0	0.0	0
c	0.037–0.003	1.11	51.3	0.18	3.0	115.6	0.36	4.6	5.08	43.3	0.0	0.0	0
a	0.040–0.056	1.19	376.5	1.27	0.8	454.6	1.49	2.0	21.57	44.0	0.0	0.0	0
c	0.040–0.056	1.09	386.0	1.17	0.3	486.2	1.67	0.7	21.06	44.0	0.0	0.0	0
b	0.041+0.060	1.09	33.7	0.19	6.9	55.0	0.15	25.7	18.16	43.1	0.0	0.0	0
a	0.042+0.082	1.12	47.0	0.30	2.0	82.1	0.47	4.2	19.30	43.5	6.2	3.6	31
c	0.042+0.082	1.32	64.4	0.19	3.9	80.4	0.22	10.0	19.61	43.2	0.0	0.0	0
b	0.044–0.033	1.15	17.9	0.24	1.5	35.2	0.21	6.3	20.43	43.2	2.7	1.2	6
a	0.051–0.165	1.88	103.9	0.93	0.7	62.4	0.50	4.2	19.86	43.7	8.2	3.9	129
c	0.050–0.165	1.31	167.5	0.50	0.6	93.5	0.40	2.2	19.61	43.5	0.0	0.0	0

Table 3. continued

	OH Name	PBF	$S_{\text{blue}}$ mJy	$I_{\text{blue}}$ <sup>a</sup>	$\epsilon$ %	$S_{\text{red}}$ mJy	$I_{\text{red}}$ <sup>a</sup>	$\epsilon$ %	$V_{\text{exp}}$ km s <sup>-1</sup>	$L_{\text{OH}}$ <sup>b</sup>	Deconvolved " "		Note <sup>c</sup>
a	0.051+0.079	1.14	39.3	0.23	2.8	81.4	0.41	4.7	19.30	43.4	3.1	2.1	172
c	0.051+0.079	1.34	83.9	0.24	1.9	129.0	0.40	3.3	18.88	43.4	0.0	0.0	0
a	0.053-0.063	1.26	63.8	0.37	1.7	128.8	0.66	2.8	17.59	43.6	2.2	1.8	142
c	0.053-0.063	1.13	76.7	0.32	1.1	238.5	1.01	1.1	18.16	43.7	0.0	0.0	0
a	0.060-0.018	1.17	193.0	1.12	1.4	684.9	1.94	2.6	19.86	44.1	0.0	0.0	0
c	0.060-0.018	1.15	156.3	1.51	0.5	692.8	2.69	0.8	19.61	44.2	0.0	0.0	0
c	0.064-0.308	2.51	107.2	0.43	1.8	103.4	0.30	7.4	16.71	43.4	0.0	0.0	0
b	0.068-0.123	1.63	57.5	0.33	1.4	43.9	0.17	8.4	17.03	43.3	0.0	0.0	0
c	0.067-0.123	1.25	82.3	0.24	1.4	53.9	0.21	5.3	17.43	43.2	0.0	0.0	0
a	0.070+0.127	1.33	81.7	0.40	2.1	246.9	1.00	2.5	18.16	43.7	0.0	0.0	0
c	0.070+0.127	1.66	77.6	0.34	1.6	263.7	1.09	1.4	17.43	43.7	0.0	0.0	0
a	0.071-0.205	2.50	1013.2	3.57	1.2	1377.4	6.27	2.0	13.62	44.6	0.0	0.0	0
c	0.070-0.205	1.57	1743.0	8.39	0.3	2788.4	13.81	0.6	13.07	44.9	0.0	0.0	0
a	0.072-0.011	1.21	56.4	0.28	1.8	24.2	0.14	10.8	16.46	43.2	0.0	0.0	0
a	0.076+0.146	1.44	227.5	0.86	1.2	642.1	1.48	2.1	21.00	44.0	0.0	0.0	0
c	0.076+0.146	1.82	316.7	1.28	0.5	948.2	2.16	0.9	21.06	44.1	0.0	0.0	0
a	0.079-0.114	1.63	551.3	1.50	0.8	287.2	1.26	2.7	14.19	44.0	0.0	0.0	0
c	0.078-0.115	1.27	525.9	2.13	0.2	355.5	1.59	0.8	13.80	44.2	0.0	0.0	0
a	0.083+0.063	1.24	153.9	0.79	0.7	66.5	0.56	3.0	19.86	43.7	0.0	0.0	0
c	0.083+0.063	1.40	139.6	0.58	0.5	57.4	0.28	3.2	19.61	43.5	4.7	1.5	176
a	0.091+0.014	1.26	31.3	0.16	3.5	59.1	0.14	11.6	7.95	43.1	0.0	0.0	0
a	0.108-0.016	1.39	87.9	0.45	1.4	60.6	0.59	3.2	21.00	43.6	4.3	1.7	3
c	0.107-0.016	1.35	60.4	0.29	3.0	45.5	0.33	7.9	19.61	43.4	0.0	0.0	0
a	0.113-0.060	1.56	455.7	2.39	0.5	400.9	2.66	1.3	17.03	44.3	2.8	2.3	142
c	0.113-0.061	1.36	452.0	2.05	0.4	446.8	2.39	1.2	17.43	44.2	0.0	0.0	0
a	0.116-0.042	1.51	31.5	0.20	3.3	72.9	0.19	10.1	18.73	43.2	0.0	0.0	0
c	0.115-0.043	1.37	27.0	0.09	5.5	54.1	0.21	8.0	17.43	43.1	0.0	0.0	0
a	0.122-0.111	1.90	101.9	0.82	0.9	80.7	0.54	4.0	17.02	43.7	8.7	2.4	161
c	0.121-0.112	1.48	126.4	0.54	1.0	110.0	0.39	4.3	17.43	43.6	0.0	0.0	0
a	0.129-0.020	1.55	177.9	0.73	1.0	40.4	0.29	7.4	18.16	43.6	7.0	1.6	164
c	0.128-0.020	1.46	256.1	0.79	1.0	70.2	0.35	6.9	18.16	43.6	0.0	0.0	0
a	0.129+0.103	1.60	601.9	2.21	1.0	1287.1	3.10	2.1	11.35	44.3	0.0	0.0	0
c	0.129+0.103	1.86	561.5	2.74	0.5	1304.6	3.65	1.1	10.90	44.4	0.0	0.0	0

Table 3. continued

	OH Name	PBF	$S_{\text{blue}}$ mJy	$I_{\text{blue}}$ <sup>a</sup>	$\epsilon$ %	$S_{\text{red}}$ mJy	$I_{\text{red}}$ <sup>a</sup>	$\epsilon$ %	$V_{\text{exp}}$ km s <sup>-1</sup>	$L_{\text{OH}}$ <sup>b</sup>	Deconvolved " "	" "	◦	Note
a	0.134–0.023	1.59	49.0	0.46	1.5	82.3	0.52	4.1	19.86	43.6	9.6	2.3	21	
c	0.134–0.023	1.49	47.8	0.34	1.0	74.6	0.23	4.5	19.61	43.3	0.0	0.0	0	
a	0.139–0.135	2.27	61.3	0.86	1.0	110.0	1.21	2.3	21.00	43.9	7.8	2.4	42	
c	0.138–0.136	1.66	91.3	0.50	1.5	164.1	0.74	3.3	21.79	43.7	0.0	0.0	0	
a	0.142+0.026	1.59	418.6	2.15	0.5	878.9	5.80	0.6	23.27	44.5	0.0	0.0	0	
c	0.141+0.026	1.63	613.3	2.93	0.2	1369.2	7.65	0.3	23.24	44.6	2.4	1.2	167	
a	0.170+0.119	2.05	113.5	0.53	2.1	74.0	0.48	6.7	22.70	43.6	4.3	2.5	174	
a	0.173+0.211	2.91	146.4	0.82	1.3	76.4	0.29	11.8	17.02	43.6	8.5	4.0	163	
a	0.178–0.055	2.14	167.6	0.74	3.1	659.2	1.67	4.2	16.46	44.0	0.0	0.0	0	
c	0.177–0.055	1.83	365.2	1.16	0.7	902.1	2.69	0.9	16.71	44.2	0.0	0.0	0	
a	0.181–0.098	2.45	71.2	0.47	1.8	161.3	1.18	2.4	18.73	43.8	5.2	3.8	152	
c	0.180–0.098	1.91	103.0	0.63	1.4	173.4	0.76	3.6	19.61	43.7	0.0	0.0	0	
a	0.189+0.053	2.09	135.3	1.27	0.7	74.0	0.76	3.4	19.86	43.9	0.0	0.0	0	
c	0.189+0.052	2.16	714.1	2.78	0.2	238.2	0.75	2.7	19.61	44.1	0.0	0.0	0	
a	0.190+0.036	2.08	1848.2	8.05	0.7	1720.4	7.03	2.4	14.18	44.8	0.0	0.0	0	
c	0.190+0.036	2.10	3109.5	16.84	0.2	3629.4	16.96	0.6	14.53	45.1	0.0	0.0	0	
a	0.200+0.232	4.01	183.4	0.70	2.2	271.6	0.90	5.2	15.89	43.8	0.0	0.0	0	
c	0.216+0.022	2.41	40.4	0.01	47.1	78.7	0.69	2.7	18.16	43.4	8.1	4.1	151	
a	0.226–0.055	2.94	.0	.00	99.0	441.9	2.05	2.9	16.65	43.9	9.6	4.9	27	ATCA
c	0.224–0.055	2.40	537.4	1.41	0.6	596.9	1.80	1.3	16.70	44.1	0.0	0.0	0	
c	0.240–0.015	2.69	135.6	0.72	1.3	121.9	0.80	3.8	18.16	43.8	0.0	0.0	0	
c	0.260–0.143	3.51	219.4	1.30	0.9	453.7	1.50	2.5	6.54	44.0	5.2	1.8	175	
c	0.264–0.078	3.25	312.1	1.70	0.8	72.3	0.48	8.7	17.43	43.9	0.0	0.0	0	
c	0.317–0.066	5.41	450.4	1.08	2.0	290.2	0.68	9.9	13.08	43.8	0.0	0.0	0	
a	0.319–0.041	8.35	1716.4	9.49	0.8	4282.4	15.30	1.4	18.16	45.0	0.0	0.0	0	
c	0.321–0.040	5.64	2557.4	13.91	0.3	5589.0	21.94	0.7	17.43	45.1	0.0	0.0	0	
c	0.333–0.138	7.47	275.7	1.16	3.9	299.1	1.44	8.7	16.71	44.0	0.0	0.0	0	
c	0.335–0.180	9.04	4597.0	17.63	0.2	3942.0	19.50	0.7	14.53	45.2	0.0	0.0	0	
a)	Units in Jy km s <sup>-1</sup>				LWHM	Peak velocity secondary in Table 2 from Lindqvist et al. (1992a)								
b)	Units in LOG (photons per second)				VLA	Peak velocity secondary in Table 2 from our VLA data								
MC	Molecular cloud complex(es)				ATCA	Peak velocity secondary in Table 2 from our ATCA data.								

In Table 2 for each entry we list in order: the survey code, the given name according to its Galactic coordinates, the measured R.A. and Declination in J2000 with the maximum error in either R.A. or Declination, the blue and red shifted velocities, the derived stellar velocity and the Galactic coordinate offsets with respect to Sgr A\*. The stellar velocity is taken as the mean of the velocities of both intensity maxima, whereas the Galactic coordinate offsets (i.e. for a “flat sky”, or  $\cos b \equiv 1$ ) is defined with respect to Sgr A\*:  $\Delta l = l_{\text{OH}} - l_{\text{Sgr A}^*}$ ,  $\Delta b = b_{\text{OH}} - b_{\text{Sgr A}^*}$ .

In Table 3 we repeat the survey code and source name, give the primary beam attenuation factor, the peak flux density and (spatially and spectrally) integrated flux together with the estimated relative integrated flux error for the blue shifted side, as well as for the red shifted side of the stellar velocity. We also list the the shell expansion velocity, and the OH maser luminosity (for an assumed isotropic radiation field and a distance of 8 kpc to the GC; Reid 1993). If the source appears to be extended, we determined an approximate deconvolved elliptical Gaussian for the source (the major axis, minor axis and position angle). The angular broadening of sources is probably caused by instrumental effects, time averaging of the visibilities or the extended background, but we cannot exclude that an extreme case of interstellar scattering of individual sources also plays a role (Van Langevelde & Diamond 1991; Van Langevelde et al. 1992b; Frail et al. 1994). The primary beam attenuation factor was calculated for both the VLA and ATCA with a polynomial, given internally in AIPS. The expansion velocity is half of the velocity separation between the maxima at both sides; however, it is not always the full extent of the feature. The blue and red shifted integrated fluxes are calculated by integrating flux densities over the channels from the stellar velocity to the first negative flux density outside the maximum.

### 3.1. The errors

Both VLA and ATCA data sets show positional offsets when compared with the positions measured by LWHM and vLJGHW. The small difference between the LWHM and vLJGHW data is due to using phase calibrators with different positional accuracies (B1730–130 and B1748–253, respectively); the LWHM and vLJGHW positions however are consistent with each other. The internal alignment of the VLA data introduced a systematic positional shift, as did the self-cal iteration of the ATCA data. Hence, there is a significant offset of a few arc-seconds between the positions measured in our VLA and ATCA image cubes. Our ATCA positions however are roughly consistent with the LWHM and vLJGHW data. We therefore attribute the systematic difference between our VLA and ATCA positions to the self-cal iteration performed to align the monitor data. Furthermore, small errors are

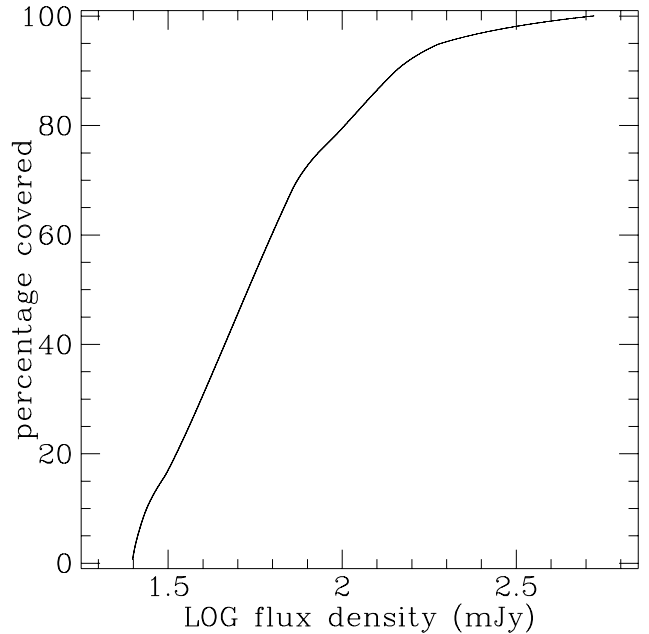


**Fig. 6.** Sky sensitivity coverage. Shown is the fraction of the surveyed sky area for which we could have detected a source of given flux density. All sources with a peak flux density over 530 mJy must have been detected; for a homogeneous distribution one reads a detection rate of 80% of the 100 mJy sources and only about 20% of the sources around 30 mJy

introduced by transforming the coordinates to (and from) epoch J2000. We stress that our *absolute* positions are not expected to be accurate at the one arc-second level. By measuring the offsets with respect to Sgr A\* (assuming no measurable relative proper motion of the OH/IR stars with respect to Sgr A\* during the monitor), however we have taken out the relative differences between our VLA and ATCA observations, and from there they can be linked to other data sets.

The positional error quoted, for a given source in a data set, is the larger of the formal errors in R.A. and Declination as derived by IMFIT in the channel with the highest peak flux density of the source. The measured positions in individual channels are consistent with the position of the source. Flux density errors are also taken from IMFIT. This relative error can be used to derive the error in the OH maser luminosity. Because the spectral features are unresolved, we can only quote the velocity resolution as estimate of the error in velocity: 1.14 (or 2.27)  $\text{km s}^{-1}$  for the VLA and 1.45  $\text{km s}^{-1}$  for the ATCA observations.

Similarly, the flux densities from the VLA data set depend on the spectral resolution used and on the effect of averaging flux densities over several epochs. OH/IR star OH flux densities and luminosities are variable, up to a factor two (e.g. Harvey et al. 1974; Herman & Habing

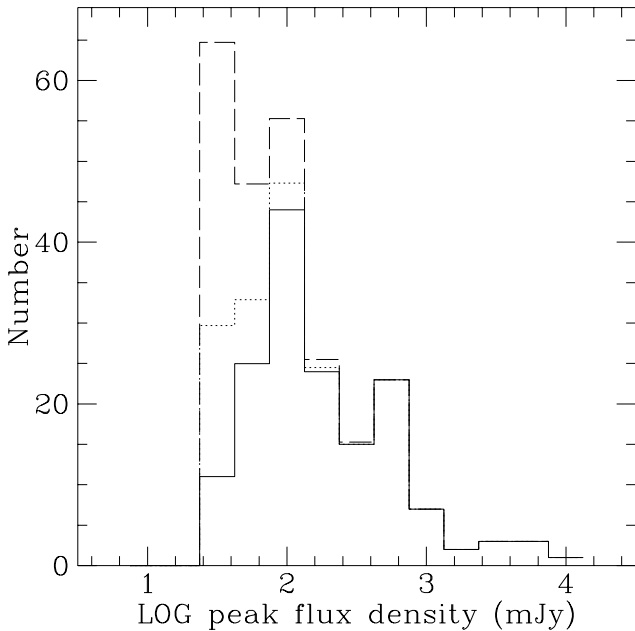


**Fig. 7.** Number distribution of peak flux densities. The dashed line gives the distribution empirically corrected for incompleteness; it is however an overestimate (see text). For example, the dotted line shows the effect on the completeness correction, when the stars are spatially distributed according to an arbitrarily scaled surface distribution  $\Sigma(R) \sim (R + R_c)^{-1}$

1985; Van Langevelde et al. 1990). The measured ATCA fluxes are therefore snapshots of the flux variability; the VLA fluxes approximate the average fluxes better, because of averaging out the amplitude variations over the monitor period. Estimating the variability effect would require detailed knowledge of the OH period and amplitude distributions and is therefore not attempted.

## 4. Discussion

### 4.1. Completeness and sensitivity

Figure 1 shows approximate contours of the best sensitivity achieved in the survey. We use it to make an empirical estimate of the (in)completeness of the survey. The number of sources detected, as function of highest peak flux density, is corrected by dividing each source by the fraction of the surveyed sky area in which it could have been found. Because the VLA and ATCA data sets have comparable spectral resolutions, we neglect the influence of channel width on the detection probability. The fraction as function of flux density can be found graphically in Fig. 6. It also shows that all sources with a peak flux density brighter than 530 mJy must have been detected (fraction = 100%, the empirical completeness limit of the survey; or more formally 390 mJy for 99%). If one would confine the area surveyed to the size of the fields used in Lindqvist

et al. (1992a, 1997), i.e. 32' squared, the completeness limit would be approximately 65 mJy. In Fig. 7 we display the number of sources with respect to the highest peak flux density, where we have given preference to the multi-epoch VLA over the one-epoch ATCA data. Because of the variable nature of the OH/IR stars, the distribution is somewhat broadened. By averaging the flux densities in the concatenated monitor data set, the effect should be smaller than in a single epoch observation. However, the exact amount of the broadening is very difficult to calculate, in particular with the mixed observations in this survey.

Strictly, this completeness correction is for a homogeneous number density distribution. As the OH/IR star distribution is concentrated toward Sgr A\*, and thus toward the survey center, we expect (and find) the largest number of *faint* stars in the part of the survey that is most sensitive. Correcting parts of the survey that are less sensitive for these faint stars, just by a linear function based on the sensitivity or geometry of the area, would then assume that pointing the telescopes far away from Sgr A\*, the detection probability of an OH/IR star is equal to the detection probability when pointing at Sgr A\*. This would imply an overestimation of the completeness correction. We have tried to show this effect in Fig. 7, by also calculating a completeness correction for an assumed number density proportional to  $r^{-2}$ , corresponding to a surface distribution  $\Sigma(R) \sim R^{-1}$  (Lindqvist et al. 1992b). It is evident that the magnitude of the effect depends on the actual concentration of stars; it cannot be extracted directly from our data.

### 4.2. Extended emission and absorption complex

Because of confusion at the location of the Sgr A complex, the survey is in practice less sensitive for detections than the actual instrumental response. As an example of the residual line emission, we show the central part of the “maxmap” of the ATCA survey in Fig. 8. Note the way the known OH/IR stars stand out with respect to the residuals. Recall that in this region a large continuum emission complex has already been subtracted. Most of the remaining line emission is located as separate spots in a ring-like shape at the inside of the supernova remnant that forms the eastern part of the Sgr A complex (e.g. Ekers et al. 1983; Pedlar et al. 1989). The few absorption measurements done in our data set, have not been explicit about the line-of-sight location of the spots with respect to the absorption and emission lines of the supernova remnant. The ring-like shape cannot be seen in individual or several consecutive frequency channels. The majority of the emission features have a velocity between 25 and 70 km s<sup>-1</sup>, placing them at, or close to either the “+50 km s<sup>-1</sup>” molecular cloud complex behind, or the “streamer” molecular cloud complex G-0.02-0.07 in front of Sgr A\* (Zylka et al. 1990). This emission may be



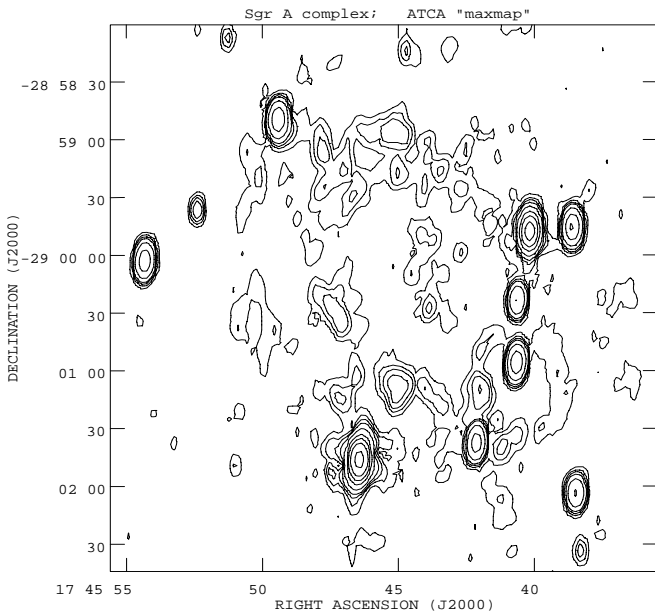


**Fig. 8.** ATCA “maxmap” of the Sgr A complex. Contours are at 0.030, 0.050, 0.070, 0.100, 0.200, 0.500, 1, 2 and 5 Jy. Sgr A\* is located in the middle of the right side of the image. The ring-like shape is due to Sgr A East and is not to be confused with the circumnuclear disk

indicative for shock fronts, where, on the near and far side of the expanding supernova shell, the shell and the molecular cloud complexes collide. This interpretation would support the recent results of the observation of shock-excited 1720 MHz OH masers by Yusef-Zadeh et al. (1996). In this region, the baselines against which we try to find double peaked OH sources are mostly irregular and make searching difficult. However, because the velocity characteristic is obvious, it is relatively easy to recognise these sources; listing all of them as single – sometimes double – peak detections, on the other hand, has not been the purpose of this survey.

Besides OH emission, the presence of OH molecules also give rise to areas of 1612 MHz absorption, which are not visible in Fig. 8 because of the “maxmap” procedure followed. We have similar “minmaps” with the detection of 1612 MHz OH absorption. Apart from the supernova remnant and other distinct regions, it is seen most pronounced in the core of the G–0.13–0.08 molecular cloud. The absorption at  $+24 \text{ km s}^{-1}$  coincides with the densest  $\text{NH}_3$  concentration in the GC, that is known to host an ultra-compact HII region, and is very close to two  $\text{H}_2\text{O}$  masers (e.g. Güsten & Downes 1983; Okumura et al. 1989). With a projected distance of only 10 parsec from Sgr A\*, it is a perfect candidate cloud to investigate present-day star formation in the GC.

#### 4.3. Remarks on individual sources

Current catalogs on OH/IR stars in the GC can be found in the appendix. When reference data is taken from LWHM, Te Lintel Hekkert et al. (1989; hereafter TLH) and Van Langevelde et al. (1992a), we (re)confirm 87 of the 89 sources that should have been visible in the ATCA data set. In the VLA data set, 67 of the 71 sources are found. An additional 3 sources, that are not (but should have been) seen in the VLA data, are confirmed in our ATCA image cube. We also confirm 4 out of 5 single peak detections of LWHM; 3 of which turn out to have a definite double peaked nature. Unconfirmed from previous surveys in the OH 1612 MHz maser line remain 4 sources: OH359.669–0.019, OH 0.204+0.056 plus the single peak OH 0.147+0.062 from LWHM, and the double peaked source OH359.897–0.065 from TLH (see the Appendix for two more non-confirmed TLH sources outside this survey).

Summarising the new detections, we find 65 previously unknown double peaked and 3 single peaked OH 1612 MHz masering sources in the VLA and ATCA surveys. We count a total of 52 previously unknown OH/IR stars. Based on a more careful examination of spatial extension and the spectral shapes, we suspect 13 detections to be molecular clouds resembling OH/IR star spectra. We confirm that all three previously known high-velocity OH/IR stars, as well as one newly found high-velocity source, are blue shifted with an absolute line-of-sight velocity exceeding  $250 \text{ km s}^{-1}$ . Because of being detectable in only one survey, we were not able to confirm 15 VLA and 11 ATCA suspected OH/IR stars ourselves. Some of these sources have, however, been detected in the infrared.

#### Non-detections

We did not confirm OH359.897–0.065 (TLH number 175); neither did LWHM. We should have seen it in the ATCA data, even when the radiation would have been in its minimum. Considering the flux density and spectrum given by Habing et al. (1983), we conclude that OH359.897–0.065 is not a real OH/IR star. Yet, one or a couple of false detections do not alter the dynamical conclusions discussed in the Habing et al. (1983) paper, or in any following article using this data point.

**OH359.669–0.019:** LWHM report a highest flux density of 0.09 Jy, which is, adjusted for the primary beam attenuation, just above our detection limit. We may have been unlucky to observe with the ATCA close to the minimum of its radiation. The source lies outside our VLA survey.

**OH 0.147+0.062:** As opposed to the other single peaks found by LWHM, for which we found a secondary peak in both surveys, this single peak has not been detected here. No counterparts were found in the literature in any other maser line or in the infrared.

**OH 0.204+0.056:** This source lies close to the edge of the survey. LWHM report a highest peak flux density of

0.11 Jy, which makes it only half of our detection threshold. The source is not covered by our ATCA survey.

#### Detections

Generally, the “overlapping” sources – i.e. sources that are in the spatial and velocity domain of both the VLA and ATCA data sets – are detected in each data set. The main cause of “overlapping” sources being detected in only the VLA data is overall sensitivity (i.e. mean flux density over several epochs); the ATCA observations were apparently done when the star was close to its minimum, and the OH maser flux density therefore below the detection limit. Backwards, sources detected only in the ATCA data are either outside the VLA cube, or the ATCA observations were apparently done when the star was close to its maximum, and the OH maser flux density therefore was larger, and above the detection limit, in contrast to the mean flux density. Following we make individual remarks on a small selection of the sources, where we use the abbreviation RR for sources in, or the paper by Rieke & Rieke (1988).

**OH359.791–0.081:** Single peak, but most likely of stellar origin because it coincides with a long period  $K$ -band variable (I.S. Glass, pers. comm.).

**OH359.797–0.025:** Either a low expansion velocity source, or the red shifted peak of a double peaked source. Not seen in the ATCA data, but the flux and shape justify its entry. Note that although we give a value for the blue shifted velocity, we cannot distinguish between a second peak and a possible effect of the end of the frequency band.

**OH359.804+0.201:** Listed as single peak in LWHM.

**OH359.837+0.052:** Listed as single peak in LWHM.

**OH359.864+0.056:** The only new source for which the absolute stellar velocity exceeds  $250 \text{ km s}^{-1}$ .

**OH359.906–0.036:** Coincides with, and matches the velocity of source #49 in RR. As for all other cases where we find an infrared counterpart for our OH maser sources, we claim the OH and infrared emission to originate from one (stellar) source.

**OH359.936–0.145:** Found as single peak by LWHM. Most probably double with the second peak at  $+13 \text{ km s}^{-1}$ , but we cannot confirm this; the source is not detected in our ATCA data.

**OH359.939–0.034:** RR report a source (#32) with a velocity of  $-14 \text{ km s}^{-1}$ . Our velocity measurement of  $+42 \text{ km s}^{-1}$  is within three times their RMS of  $20 \text{ km s}^{-1}$ . Taking into account the spatial extension of the emission, we are however tempted to attribute the OH emission to molecular clouds on the line-of-sight. If one supposes the velocity of RR is very accurate, one can argue that source #32 can be seen in the OH spectrum with two peaks of  $\approx 15 \text{ mJy}$ , separated by about  $10 \text{ km s}^{-1}$ .

**OH359.943–0.055:** Matches the velocity of the nearby source GCIRS 19 (Sellgren et al. 1987; source #22 in RR), but we doubt the identification as such. Besides, GCIRS 19 is classified as probably being a supergiant (most recently

by Blum et al. 1996), for which one would expect a shell expansion velocity larger than the  $6.5 \text{ km/s}$  found here.

**OH359.947–0.046:** Although our absolute positions are not expected to be very accurate (see Sect. 3.1), our VLA position for this source agrees within one arcsecond of the position of GCIRS 5. The velocity measured matches the one given in Krabbe et al. (1991) and Haller et al. (1996). We propose this source to be the OH counterpart for GCIRS 5. Note that the OH maser reveals a low shell expansion velocity, hinting toward a low metallicity, and low mass AGB star.

**OH359.954–0.041:** The clearest example of interesting spectral structure seen in some (of the stronger) OH/IR stars in the GC. We discuss these peculiar spectra further in Sect. 4.5.

**OH359.956–0.050:** Found as an  $\text{H}_2\text{O}$  maser by Levine et al. (1995) and Yusef-Zadeh & Mehringer (1995). Its nature – a young, massive supergiant or an evolved, intermediate mass AGB star – has been extensively discussed in Sjouwerman & Van Langevelde (1996). The AGB nature of this object, identified with GCIRS 24 as its infrared counterpart, has been supported recently by Blum et al. (1996), and was initially motivated by Sellgren et al. (1987).

**OH359.957–0.123:** A single peak detection, but probably stellar: it has been identified with a long period  $K$ -band variable (I.S. Glass, pers. comm.).

**OH359.965–0.043:** The SIMBAD data base reports this position to be close to the position of IRC–30321. However, the error in the position of IRC–30321 is large ( $\sim 1'$ ) and we therefore find it more likely that IRC–30321 coincides with one of the other nearby luminous (previously known) OH/IR stars instead.

**OH359.970–0.049:** On top of the extended emission we find a double peaked point source. It has most probably been detected by LWHM as their source #69. LWHM apparently mistook a peak of (the molecular cloud) OH359.970–0.047 as their secondary peak velocity, resulting in a relatively high value for the shell expansion velocity. More likely than OH359.970–0.047, this source seems to be related to source #38 in RR. They give a velocity of  $109 \text{ km s}^{-1}$  with an RMS of  $20 \text{ km s}^{-1}$  where we measured  $89 \text{ km s}^{-1}$ .

**OH359.971+0.068:** Listed as single peak in LWHM.

**OH359.980–0.077:** Found as an  $\text{H}_2\text{O}$  maser by Yusef-Zadeh & Mehringer (1995), but in fact an OH/IR star; see discussion in Sjouwerman & Van Langevelde (1996).

**OH359.985–0.042:** RR found a source (#51) at  $-55 \text{ km s}^{-1}$ , three times their RMS away from our velocity. However, we are confident that the identification of the OH source with source #51 in RR fits.

**OH359.990+0.030:** This source lies close to IRAS 17423–2855. Te Lintel Hekkert & Chapman (1996) searched IRAS 17423–2855 for OH emission, but did not find it because of a noise level of  $440 \text{ mJy}$ . The position of OH359.990+0.030 is however more than  $20''$  off from

the positions given for several possible near-infrared counterparts for IRAS 17423–2855 in Monetti et al. (1992). Although IRAS 17423–2855 can also be interpreted as an ultra-compact HII region, the association with double peaked OH emission is more convincing for a (post-)AGB object (e.g. Volk & Cohen 1989; Monetti et al. 1994; Te Lintel Hekkert & Chapman 1996).

**OH 0.001+0.353:** A source named OH359.984+0.349 in TLH (#155), observed by Habing et al. (1983) with the 100 m single dish telescope in Effelsberg (Bonn). We confirm the position measured by LWHM; it differs about one arcminute from the position quoted in TLH.

**OH 0.005+0.360:** Because of its spectral shape and because it is not spatially resolved, we suspect this source to be the red shifted peak of a double peaked OH/IR source.

**OH 0.014–0.046:** Close to, and maybe related to the infrared source GCS 6 in Kobayashi et al. (1983).

**OH 0.053–0.063 and OH 0.060–0.018:** The former was marked by LWHM as detected by Winnberg et al. (1985); it should have been the latter.

**OH 0.064–0.308:** Located near a compact HII region (#16 in Downes et al. 1979).

#### 4.4. Comparison with known OH/IR stars

The OH/IR stars found for the first time in this survey have less luminous OH masers in their circumstellar shells compared to the previously known OH/IR stars in the GC. In this section we argue that the newly found stars are of similar nature to the ones previously known. This result was used in Sjouwerman & Van Langevelde (1996).

##### 4.4.1. Spatial and kinematic distribution

Figures 2 and 3 show the spatial and kinematic distribution of the known and previously unknown OH/IR stars detected in this survey. It is clear in Fig. 2, that the more luminous OH masers, generally the known OH/IR stars, can also be detected further out from the survey center. The fact that there are more stars at positive latitude offsets is an effect of the asymmetry in the survey pointing. Where the survey is sensitive enough, one sees that there is no preferred, and no distinct location for each of the samples. However, we make the observation that the alleged void of known OH/IR stars at small positive longitudes and small positive latitudes, does not comply with the combined sample. Furthermore, a comparison of the location of stars in Fig. 2 and Fig. 3 between both samples also suggests a similar distribution in phase-space.

##### 4.4.2. Expansion velocity distribution

To argue further that the samples consist of the same type of stars, we show the distributions of the shell expansion

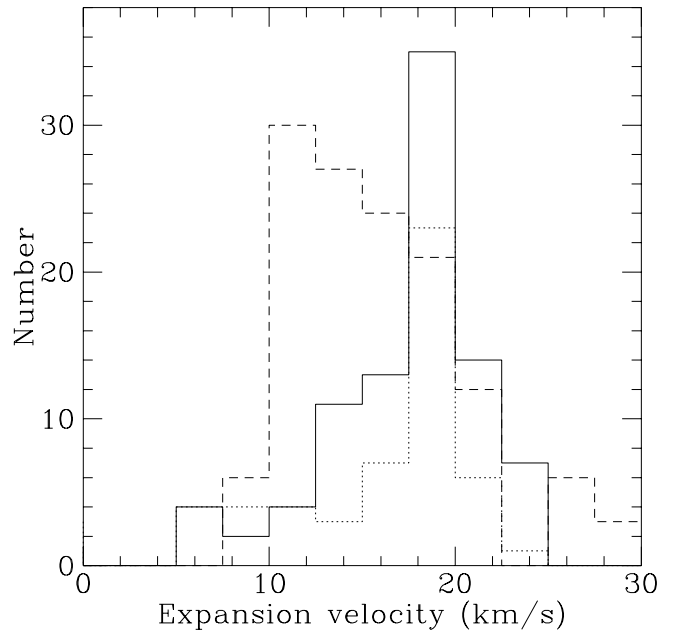


**Fig. 9.** Expansion velocity distribution. The solid line is the distribution of previously known OH/IR stars in our survey, new detections are distributed according to the dotted line. The striking resemblance of both distributions is in large contrast to the expansion velocity distributions of OH/IR stars with a different metallicity, for example in the outer Galaxy and Galactic plane (dashed: Blommaert et al. 1993 plus Blommaert et al. 1994, multiplied by three for display purposes)

velocity in Fig. 9. Both samples<sup>3</sup> have shell expansion velocities sharply peaked around 19 km s<sup>-1</sup>. Expansion velocity distributions for many other samples of OH/IR stars can be found in the literature, e.g. Eder et al. (1988), Te Lintel Hekkert et al. (1991) and Wood et al. (1992). We want to restrict ourselves by comparing the expansion velocities of the OH/IR star in the GC with samples of the Galactic plane (Blommaert et al. 1993, 1994) and the Galactic bulge (Sevenster et al. 1997).

The distribution of the OH/IR stars found in the Galactic plane is also shown in Fig. 9. The distribution for the Galactic bulge has its peak around 15 km s<sup>-1</sup>, and is broader than for the GC (see Sevenster et al. 1997). When comparing the expansion velocities of the OH/IR stars in the GC with the ones in the Galactic plane and bulge, we reach two conclusions. First, the expansion velocity distribution in the GC is different from the expansion velocity distribution of any other sample known, which we attribute to generally higher metallicities in the GC (see the discussions in e.g. Wood et al. 1992; Blommaert et al. 1994 and Habing 1996). Second, we note the striking

<sup>3</sup> Note that we do not include all stars found in the whole GC region in our analysis; only the stars detected in this survey.

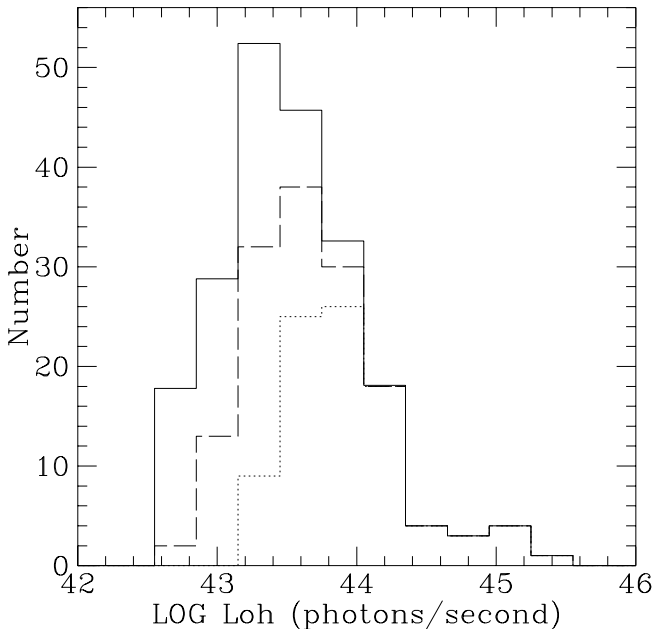


**Fig. 10.** OH luminosity distribution. The dashed curve combines the previously known OH/IR stars in our survey and the new detections. The known OH/IR star luminosity distribution is depicted by the dotted line. The solid line outlines the maximum extent of the distribution, i.e. corrected for incompleteness according to a homogeneous spatial distribution

resemblance of the expansion velocity distribution of the known and the previously unknown OH/IR stars in this survey, and argue for generally *identical* metallicities for both of our samples. Hence, as the shell expansion velocity is a function of metallicity and stellar luminosity, we conclude that the stellar luminosity distribution for both of our samples is identical; as far as we can tell, the central stars are the same.

#### 4.4.3. OH maser luminosity function

Because both the known and previously unknown OH/IR stars are intrinsically identical, we can investigate the combined OH luminosity distribution. Figure 10 shows the result when we assume that all stars are located at a distance of 8 kpc. That the new detections are mainly the low OH luminosity sources can be seen readily from the difference in the total distribution and the known OH/IR star distribution. Also shown is the *maximum* extent of the distribution when it is corrected for (in)completeness. We calculated this correction by weighing each source by the inverse of its detection probability and assuming a homogeneous number distribution.

Again, this correction is an overestimate. Unfortunately the number of sources with respect to the corrections at the left-hand side of the luminosity distribution is small. In general these are the sources with a low peak

flux density for which the survey is not complete. It prevents us to derive a firm conclusion about a possible low luminosity cut-off in the OH maser distribution. We can however state, that the distribution peaks at  $L_{\text{OH}} \approx 10^{43.4}$  photons per second within the statistical errors.

#### 4.5. Triple and quadruple maser lines

In Sect. 4.3 we mentioned non-standard spectral structure seen in OH359.954–0.041 (a category 1 OH variable in vLJGHW). Less clear examples, both variable (cat. 1, 2) and non-, or irregularly variable<sup>4</sup> (cat. 3) sources, are OH359.675+0.070 (cat. 2), OH359.879–0.087 (cat. 1), OH359.938–0.052 (cat. 2), OH 0.040–0.056 (cat. 3), OH 0.076+0.146 (cat. 1), OH 0.083+0.063 (not monitored), OH 0.142+0.026 (cat. 1) and OH 0.319–0.041 (cat. 3). The masers in OH359.954–0.041 and OH 0.040–0.056 are quadruple peaked, the rest are triple peaked. In addition to the “a” spectra in Fig. 5, Fig. 11 shows the lower frequency resolution spectra measured in image cube “b” for four of these stars. We have only seen this type of spectra in the concatenated data; spectra with *regular* additional emission features at roughly either 15 or 50 km s<sup>−1</sup> on the redshifted side of the redshifted peak, or about 15 km s<sup>−1</sup> “outside” both main peaks. Instrumental effects (e.g. the Gibbs phenomenon) and side-lobe features of nearby sources can be excluded.

In the case of OH359.954–0.041 we measured a consistent positional offset of 1.34 arcsecond ( $\sim 10\,000$  AU, or 10 times the shell radius that was measured from the phase-lag of the main peaks by vLJGHW) to the southwest, from the main peaks to both outer peaks. The 61 km s<sup>−1</sup> feature “inside” the main peaks is positionally coincident with the main peaks. The outer peaks of OH 0.040–0.056 are displaced about 0.6” northeast from the main peaks, again within the errors at mutual excluding positions. Because of the symmetry seen in OH359.954–0.041, and in OH 0.040–0.056, and the rather remarkable velocity interval structure in all examples, we tend to conclude that the emission is from (the shell of) the OH/IR star itself; not from another source (an OH/IR binary, or more exotically, an OH/IR star captured by an OH masering supergiant) seen at the same projected coordinates. Suggestions then range from a double shell, indicating different epochs of interrupted mass-loss as seen for carbon rich AGB stars (Olofsson et al. 1996), creation of other molecules besides CO already early in the mass-loss history, an effect related or similar to the mode switching seen in the H<sub>2</sub>O maser lines of OH 39.7+1.5 (Engels et al. 1997), to bipolar outflow. These stars clearly make excellent test-cases for our understanding of the mass-loss mechanism of evolved stars.

<sup>4</sup> However, OH 0.040–0.056 and OH 0.079–0.114 were found to be regularly variable in the infrared by Jones et al. (1994). OH 0.319–0.041 was not in their sample.

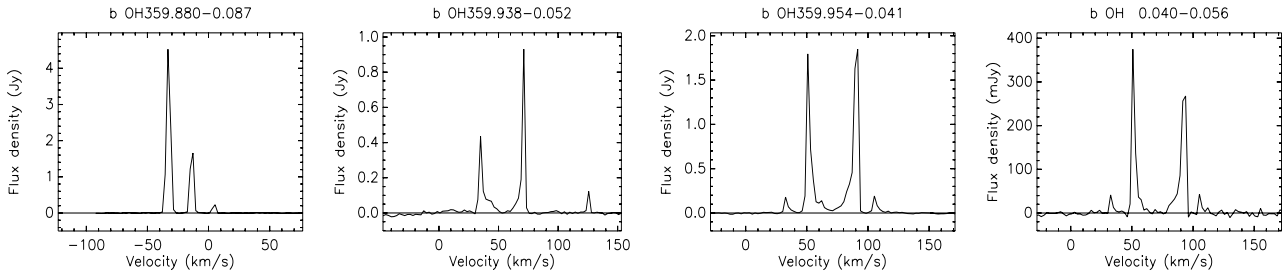


**Fig. 11.** Spectra from image cube “b” for selected sources. See Sect. 4.5

Although the both uniformly sampled VLA and ATCA data sets have a comparable sensitivity, the spectral features are only clearly seen in the concatenated VLA data set. Therefore the features result from either weak emission from many epochs, or strong emission at a limited amount of individual epochs. Making a case for the latter, other examples of similar, one epoch spectra in the literature can be found, however undiscussed, in Te Lintel Hekkert et al. (1991; IRAS 15452–5459 and IRAS 17253–2824), and in Sevenster et al. (1997; e.g. OH353.421–0.894, OH 2.186–1.660 and OH 5.991+0.252). Furthermore, Eder et al. (1988) mention an identical phenomenon in IRAS 18520+0533 (OH 38.3+1.9), and suggest it to be mapped. However, OH 38.3+1.9 was found unresolved at 1612 MHz with the VLA in CD-array by Lewis et al. (1990), and observations with the European VLBI Network have not been published yet (M. Lindqvist, pers. comm.). Note however, that this OH emission of OH359.954–0.041 and OH 0.040–0.056 cannot be detected with VLBI observations, because of severe scattering of the source at decimeter wavelengths ( $0.6''$  at 1612 MHz for OH359.954–0.041; Van Langevelde et al. 1992b).

## 5. Conclusions

We detected 155 double peaked 1612 MHz sources within  $18'$  of Sgr A\*. Of the 155 detections, 52 are previously unknown OH/IR stars. In addition, 3 single peak detections are given, which are most probably masers of OH/IR stars as well. We have also listed 13 double peaked sources that exceed the RMS noise levels by a factor of 8, and that most probably originate in the molecular cloud complex located at the GC. The sky and velocity distribution, as well as the expansion velocity distribution of the low OH luminosity stars compare very well with the previously known OH/IR stars in the GC. We therefore conclude that this survey revealed the low OH luminosity part of the GC OH/IR star population; the additional sources in the new sample are intrinsically identical to the AGB stars of the known sample, except for a less efficient OH maser. The OH/IR star OH maser luminosity distribution peaks at

$L_{\text{OH}} \approx 10^{43.4}$  photons per second. From this survey however, we can not conclude with certainty that there is a low luminosity cut-off of the OH maser luminosity distribution.

*Acknowledgements.* LOS hereby thanks all who made it possible to have this unusually large data set concatenated and analysed; in particular everyone at Sterrewacht Leiden for avoiding the local area network during nighttime, and the AIPS users in Onsala for flexible disk space usage. Thanks to Ian Glass for providing data before publication and to Michael Lindqvist for his continuous interest. For this project LOS received financial support from Sterrewacht Leiden, Svenska Institutet and Onsala Rymdobservatorium. HJvL acknowledges support for his research by the European Union under contract CHGECT920011 and AW acknowledges support by the Swedish Natural Science Research Council. In this article we use observations obtained with the Australia Telescope, which is funded by the Commonwealth of Australia for operation as a National Facility managed by CSIRO, and data collected with the Very Large Array, operated as part of the National Radio Astronomy Observatory by Associated Universities Inc. under cooperative agreement with the National Science Foundation. This research has made use of the SIMBAD database, operated at CDS, Strasbourg, France.

## A. Appendix: Catalogs

For the identification of OH/IR stars in the Galactic center (GC), the catalog of Lindqvist et al. (1992a; LWHM) is the most complete. The pre-IRAS *catalogue of stellar 1612 MHz maser sources*, compiled from the literature by Te Lintel Hekkert et al. (1989; TLH), lists additional GC stellar OH maser sources that lie outside the area or velocity coverage surveyed by LWHM. However, LWHM did not confirm two sources in the TLH catalog: OH359.897–0.065 and OH 0.482–0.164 (TLH numbers 175 and 207). Source OH359.897–0.065 has been discussed in Sect. 4.3. For OH 0.482–0.164 (TLH#207) TLH give three references: Baud et al. (1979), Baud et al. (1981) and Olon et al. (1981). The latter however, use the data of Baud et al. (1979).

We noticed that in Baud et al. (1979), comparing with Baud et al. (1981), the velocity and flux data corresponding to OH 0.482–0.164 (OH 0.48–0.13 or OH 0.5–0.1) has

been entered for OH 0.503–0.758 (OH 0.5–0.8) and vice versa<sup>5</sup>. Source OH 0.482–0.164 has been confirmed by Habing et al. (1983) and LWHM at the “proper” (i.e. Baud et al. 1981) velocities; source OH 0.503–0.758 has probably been detected as an H<sub>2</sub>O maser (with a velocity of  $-58 \text{ km s}^{-1}$ ; Batchelor et al. 1980 — who, however, did not recognise it as a stellar source), as a signal accidentally picked up in a single dish beam pointed towards the HII region G 0.55–0.85 (e.g. Downes et al. 1979). There are no confirmations the other way around. Therefore, the data listed in Baud et al. (1979) should be read as in Baud et al. (1981). This means therefore also, that the velocity and flux data for TLH#207 and TLH#214 should be exchanged. Hence, it appears that TLH#206 and TLH#207, respectively TLH#213 and TLH#214, are entries for the same sources.

Most surveys for OH/IR stars after 1983 are based on the IRAS Point Source Catalog data base, exploiting the highly successful predictive property of the IRAS two-colour diagram for detecting OH/IR stars (Olson et al. 1984; Van der Veen & Habing 1988). Because of confusion in the GC, these surveys omit the GC area (however, see Taylor et al. 1993 for a description of an “IRAS Galactic Center Catalog”).

Additionally to the data listed in TLH and LWHM, two other 1612 MHz surveys covering the GC have been done. Van Langevelde et al. (1992a) found two high-velocity OH/IR stars in the GC, and Sevenster et al. (1997) filled the gap of the GC and bulge, where the IRAS survey had suffered from confusion. Because the latter survey has a low sensitivity compared to LWHM, in particular in the GC region, no new matches were found.

We also extended our search for possible stellar counterparts for our new detections in other wavelength regions. Many matches were found in a preliminary list of long period *K*–band variables, kindly provided by Ian Glass (for a description see Glass et al. 1996). New detections were cross-correlated with the SIMBAD data base ( $\lesssim 20''$  radius), and with data sets found in the main journals between 1979 and 1996. However, in general the overlap is minimal.

## References

- Batchelor R.A., Caswell J.L., Goss W.M., Haynes R.F., Knowles S.H., Wellington K.J., 1980, *Aust. J. Phys.* 33, 139
- Baud B., Habing H.J., Matthews H.E., O’Sullivan J.D., Winnberg A., 1975, *Nat* 258, 406
- Baud B., Habing H.J., Matthews H.E., Winnberg A., 1979, *A&AS* 35, 179
- Baud B., Habing H.J., Matthews H.E., Winnberg A., 1981, *A&A* 95, 171
- Blommaert J.A.D.L., van der Veen W.E.C.J., Habing H.J., 1993, *A&A* 267, 39
- Blommaert J.A.D.L., van Langevelde H.J., Michiels W.F.P., 1994, *A&A* 287, 479
- Blum R.D., Sellgren K., DePoy D.L., 1996, *AJ* 112, 1988
- Cornwell T.J., Uson J.M., Haddad N., 1992, *A&A* 258, 583
- Dejonghe H., 1993, in: *Galactic bulges*, Dejonghe H., Habing H.J. (eds.). Kluwer Academic Publishers, Dordrecht, p. 73
- Downes D., Goss W.M., Schwarz U.J., Wouterloot J.G.A., 1979, *A&AS* 35, 1
- Eder J., Lewis B.M., Terzian Y., 1988, *ApJS* 66, 183
- Ekers R.D., van Gorkom J.H., Schwarz U.J., Goss W.M., 1983, *A&A* 122, 143
- Engels D., Winnberg A., Walmsley C.M., Brand J., 1997, *A&A* (in press)
- Frail D.A., Diamond P.J., Cordes J.M., van Langevelde H.J., 1994, *ApJ* 427, L43
- Glass I.S., Matsumoto S., Ono T., Sekiguchi K., 1996, in: *The Galactic Center*, Gredel R. (ed.) PASPC 102, 312
- Güsten R., Downes D., 1983, *A&A* 117, 343
- Habing H.J., 1993, in: *Galactic bulges*, Dejonghe H., Habing H.J. (eds.). Kluwer Academic Publishers, Dordrecht, p. 57
- Habing H.J., 1996, *A&AR* 7, 97
- Habing H.J., Olson F.M., Winnberg A., Matthews H.E., Baud B., 1983, *A&A* 128, 230
- Haller J.W., Rieke M.J., Rieke G.H., Tamblyn P., Close L., Melia F., 1996, *ApJ* 456, 194
- Harvey P.M., Bechis K.P., Wilson W.J., Ball J.A., 1974, *ApJS* 27, 331
- Herman J., Habing H.J., 1985, *A&AS* 59, 523
- Iben I., Renzini A., 1983, *ARA&A* 21, 271
- Jones T.J., McGregor P.J., Gehrz R.D., Lawrence G.F., 1994, *AJ* 107, 1111
- Kobayashi Y., Okuda H., Sato S., Jugaka J., Dyck H.M., 1983, *PASJ* 35, 101
- Krabbe A., Genzel R., Drapatz S., Rotaciuc V., 1991, *ApJ* 382, L19
- Levine D.A., Figer D.F., Morris M., McLean I.S., 1995, *ApJ* 447, L101
- Lewis B.M., Chengalur J.N., Schmelz J., Terzian Y., 1990, *MNRAS* 246, 523
- Lindqvist M., Winnberg A., Habing H.J., Matthews H.E., 1992a, *A&AS* 92, 43 (LWHM)
- Lindqvist M., Habing H.J., Winnberg A., 1992b, *A&A* 259, 118
- Lindqvist M., Winnberg A., Habing H.J., 1997 (in preparation)
- Monetti A., Glass I.S., Moorwood A.F.M., 1992, *MNRAS* 258, 705
- Monetti A., Glass I.S., Moorwood A.F.M., 1994, *MNRAS* 268, 194
- Okumura S.K., Ishiguro M., Fomalont E.B., et al., 1989, *ApJ* 347, 240
- Olson F.M., Walterbos R.A.M., Habing H.J., et al., 1981, *ApJ* 245, L103
- Olson F.M., Baud B., Habing H.J., de Jong T., Harris S., Pottasch S.R., 1984, *ApJ* 278, L41
- Olofsson H., Bergman P., Eriksson K., Gustafsson B., 1996, *A&A* 311, 587
- Pedlar A., Anantharamaiah K.R., Ekers R.D., Goss W.M., van Gorkom J.H., Schwarz U.J., Zhao J.-H., 1989, *ApJ* 342, 769
- Reid M.J., 1993, *ARA&A* 31, 345
- Rieke G.H., Rieke M.J., 1988, *ApJ* 330, L33 (RR)
- Sellgren K., Hall D.N.B., Kleinmann S.G., Scoville N.Z., 1987, *ApJ* 317, 881

<sup>5</sup> In the first chapter of Baud’s thesis, a preliminary version of the 1979 paper, this exchange had not yet occurred.

- Sevenster M.N., Dejonghe H., Habing H.J., 1995, *A&A* 299, 689
- Sevenster M.N., Chapman J.M., Habing H.J., Killeen N.E.B., Lindqvist M., 1997, *A&AS* 122, 79
- Sjouwerman L.O., van Langevelde, H.J., 1996, *ApJ* 461, L41
- Taylor G.B., Morris M., Schulman E., 1993, *AJ* 106, 1978
- te Lintel Hekkert P., Versteeg-Hensel H.A., Habing H.J., Wiertz M., 1989, *A&AS* 78, 399 (TLH)
- te Lintel Hekkert P., Chapman J.M., 1996, *A&AS* 119, 459
- te Lintel Hekkert P., Caswell J.L., Habing H.J., Haynes R.F., Norris R.P., 1991, *A&AS* 90, 327
- van der Veen W.E.C.J., Habing H.J., 1988, *A&A* 194, 125
- van Langevelde H.J., van der Heiden R., van Schooneveld C., 1990, *A&A* 239, 193
- van Langevelde H.J., Cotton W.D., 1990, *A&A* 239, L5
- van Langevelde H.J., Diamond P.J., 1991, *MNRAS* 249, 7P
- van Langevelde H.J., Brown A.G.A., Lindqvist M., Habing H.J., de Zeeuw P.T., 1992a, *A&A* 261, L17
- van Langevelde H.J., Frail D.A., Cordes J.M., Diamond P.J., 1992b, *ApJ* 396, 686
- van Langevelde H.J., Janssens A.M., Goss W.M., Habing H.J., Winnberg A., 1993, *A&AS* 101, 109 (vLJGHW or the “monitor”)
- Volk K., Cohen M., 1989, *AJ* 98, 931
- Whitelock P., Feast M., Catchpole R., 1991, *MNRAS* 248, 276
- Winnberg A., Baud B., Matthews H.E., Habing H.J., Olton F.M., 1985, *ApJ* 291, L45
- Wood P.R., Whiteoak J.B., Hughes S.M.G., Bessell M.S., Gardner F.P., Hyland A.R., 1992, *ApJ* 397, 552
- Yusef-Zadeh F., Roberts D.A., Goss W.M., Frail D.A., Green A.J., 1996, *ApJ* 466, L25
- Yusef-Zadeh F., Mehringer D.M., 1995, *ApJ* 452, L37
- Zylka R., Mezger P.G., Wink J.E., 1990, *A&A* 234, 133